

Lappeenranta-Lahti University of Technology LUT

School of Engineering Science

Degree Programme in Technical Physics

Mariia Vinogradova

**AFM investigation of the influence of relative humidity on the electrical potential of tin oxide films**

Examiners: Professor Erkki Lähderanta

D.Sc. (Technology) Pavel Geydt

Supervisors: Professor Erkki Lähderanta

D.Sc. (Technology) Ekaterina Soboleva

D.Sc. (Technology) Pavel Geydt

## **ABSTRACT**

Lappeenranta-Lahti University of Technology LUT

School of Engineering Science

Degree Programme in Technical Physics

Mariia Vinogradova

### **AFM investigation of the influence of relative humidity on the electrical potential of tin oxide films**

Master's thesis

2021

65 pages, 57 figures, 6 tables

Examiners: Professor Erkki Lähderanta

D.Sc. (Technology) Pavel Geydt

Keywords: AFM, KPFM, tin films, relative humidity, potential

The influence of the relative humidity (RH) of the air on the electric potential of the materials' surfaces was investigated. Nickel-doped tin dioxide films were synthesized by magnetron sputtering in argon plasma. Atomic Force Microscope (AFM) was used for the experiments. The electric potential of the films and their topography were measured by Kelvin Probe Force Microscopy (KPFM). During the measurements, the humidity was varied cyclically. The humidity setup consisted of a tube system, bubbler, and humidity sensor connected to an Arduino Uno motherboard. The analysis of the data obtained was carried out, comparative histograms for different humidity levels were presented. As a result, it was shown that the film potential changes with a change in RH, although no strict correlation was found between these values.

## **ACKNOWLEDGEMENTS**

By this work, I am thankful to my professor Erkki Lähderanta for welcoming me at one of the most respectful and prestigious institutes, Lappeenranta-Lahti University of Technology LUT. His guidance set forth the research field of technical physics to my education, establishing the basis for the following contribution.

The project on master's thesis introduced me to Ekaterina Soboleva and Pavel Geydt to whom I am grateful for the directions on conducting the experiments, suggestions and support on carrying out my research. These experiments would not be possible without the financial support from LUT University who provided the scholarship for my studies.

I would like to thank Electrotechnical University "LETI" for the given opportunity to study on a double-degree program. This would not have been possible without the knowledge, experience, and skill I acquired with the help of my professors during my studies.

I also express my gratitude to Belarus State University, especially to V. Ksenevich for the offered experimental samples and conducted research.

Lappeenranta, May 2021

Mariia Vinogradova

## Table of content

List of Symbols .....	5
List of Abbreviations .....	6
1. Introduction.....	7
2. Literature review .....	8
2.1. Atomic Force Microscopy .....	8
2.1.1. Basic components of an AFM .....	10
2.1.2. Modes of operation of an AFM .....	13
2.2. Kelvin Probe Force Microscopy .....	15
2.3. The physical concept of converting humidity to electricity.....	17
2.4. Related works .....	23
3. Measurement procedure.....	27
3.1. NanoScope Software.....	27
3.1.1. Measurements in Nanoscope software .....	27
3.1.2. NanoScope Analysis Software.....	31
3.2. Equivalent electrical circuit of measurements .....	32
3.3. Synthesis of tin dioxide films with clusters of ferromagnetic metals.....	33
3.4. Experimental setup .....	35
4. Measurement results .....	37
4.1. Sample #1 with 4 mm Ni and 0% O <sub>2</sub> .....	37
4.2. Sample #2 with 4 mm Ni and 4% O <sub>2</sub> .....	46
4.3. Sample #3 with 2 mm Ni and 0% O <sub>2</sub> .....	53
5. Conclusion .....	61
References.....	63

## List of Symbols

$\phi_s$	Work function of the sample
$\phi_t$	Work function of the probe
$\phi(x)$	Surface potential
$A$	Amplitude of the Gaussian peak
$C(z)$	Capacitance of the probe-sample system
$C_{air}$	Air Capacitance
$C_{sw}$	Sample Wafer Capacitance
$d$	Distance between probe and sample
$F$	Force of interaction
$F_{cap}$	Capacitive force between probe and surface
$F_L$	Lateral component of the force of interaction between the probe and surface
$F_Z$	Z-component of attractive or repulsive force
$i$	Current
$k$	Spring constant of the cantilever
$R_c$	Silver Conductive Paste Resistance
$R_f$	Tin Film Resistance
$R_p$	Probe Resistance
$R_w$	Metal Wafer Resistance
$S$	Surface sites
$V_{ac}$	Supplied AC voltage
$V_{CPD}$	Contact potential difference
$V_{dc}$	Supplied DC voltage
$V_{tip}$	Total voltage applied to the probe
$w$	Width of the Gaussian peak
$x$	Cantilever displacement from its normal position
$X_c$	Center Value of the Gaussian peak
$y_0$	Offset of the Gaussian peak

## List of Abbreviations

AFM	Atomic Force Microscopy/ Atomic Force Microscope
KPFM	Kelvin Probe Force Microscopy
OM	Optical Microscope
PSD	Position-Sensitive Detector
RH	Relative Humidity
SPM	Scanning Probe Microscopy
T-M	Tetragonal-Monoclinic phase

## 1. Introduction

The question of producing energy from the renewable sources is acute at present. At the moment, such alternative energy sources as solar energy, wind energy, hydropower, and geothermal energy are well studied and widely used. For all the above-mentioned "sources" there are already some prototypes or devices that can produce an electric current. However, moisture can be another source of renewable energy. The concept of converting moisture to electricity has not yet been explored. There are no prototypes of humidity-to-electricity converters yet and materials suitable for these devices have not been investigated either. Thus, the study of such materials is a promising direction in the development of alternative energy.

The framework provided in the previous projects attempted to investigate the phenomenon of producing this type of energy, introduced the discussion on the principles of the humidity to electricity converter technology (Ducati, Simões and Galembeck, 2010a; Doroshkevich *et al.*, 2017). It has been shown that some materials can change their potential due to changes in RH (Rasheed, 2017). Nevertheless, a particular surface potential and charge distribution measurements are required to provide a better understanding of the conversion process. Such measurements are enabled with the use of AFM. The well-known advantage of AFM is in high atomic resolution and availabilities to obtain several properties (e.g. the sample surface potential) simultaneously during one scan without unnecessary damages of the sample structure.

Based on the studied earlier projects in this field, there is a hypothesis suggesting a fluctuation in film potential correlating with a change of relative humidity. To test this, tin-based films are measured using a KPFM. This thesis attempts to elaborate on the hypothesis and therefore consists of the following five main parts.

In the second part "Literature Review" the main provisions, principles of AFM operation, and basic modes are considered. Possible physical concepts of converting humidity to electricity, and related works and their results, are also described. The third part "Measurement Procedure" provide information about the sample synthesis, measurement setup and used software. The fourth part "Measurement results" presents and describes the experimental results. The last fifth part is a "Conclusion", where the obtained results are discussed and recommendations for further measurements are given.

## 2. Literature review

### 2.1. Atomic Force Microscopy

Atomic Force Microscope (AFM) belongs in the Scanning Probe Microscope family (SPM) to the branch of scanning force microscopy. The family microscopy tree is shown in Figure 1. The foundations of SPM were laid in the 1980s by Swiss scientists Dr. Gerd Binnig and Dr. Heinrich Rohre. In 1981, they created the first Scanning Tunneling Microscope and in 1986 received the Nobel Prize for this invention (Rugar and Hansma, 1990). In 1985 Dr. Binnig, Dr. Christoph Gerber, and Dr. C. F. Quate developed AFM, and in 1987 Tom Albrecht was able to get the first image of a single atom. In 1988 AFM became available for commercial use (Verma and Singh, 2020).

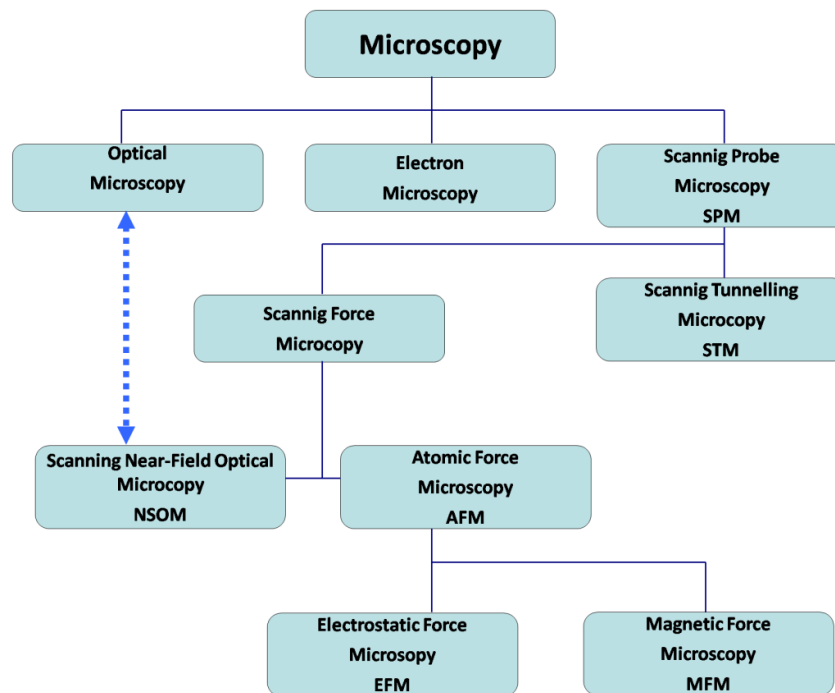


Figure 1. The family microscopy tree.

The working principle of AFM is to measure the interaction force between a sample and microscope probe (Giessibl, 2003). The probe is attached to a cantilever that bends when a force is applied to it. A laser beam falls on the end of the cantilever and is reflected back to a photodiode (Figure 2). The photodiode has four sections. Before starting measurements, the optical detecting system of AFM is calibrated so that the laser beam hits the center of the photodiode. During the measurements, when the cantilever is deflected, the laser beam is

displaced relative to the center of the photodiode. This allows the deflection to be recorded and is used for the controlling feedback system. Thus, it is possible to judge the magnitude of the interaction force between the sample and the probe.

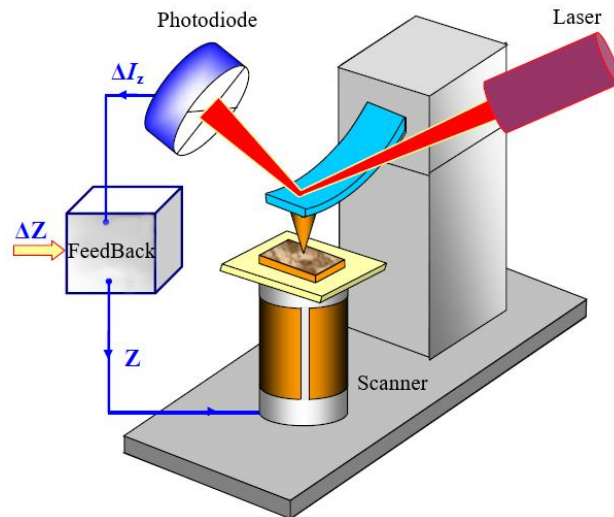


Figure 2. Schematic representation of Atomic Force Microscope (Mironov, 2004).

A schematic representation of a four-sectioned position-sensitive detector (PSD) is shown in Figure 3. The figure shows how the deformation of the cantilever affects the position of the laser spot incident on the photodiode.  $F_z$  is the Z-component of attractive or repulsive force and  $F_L$  is the lateral component of the force of interaction between the probe and surface (Mironov, 2004).

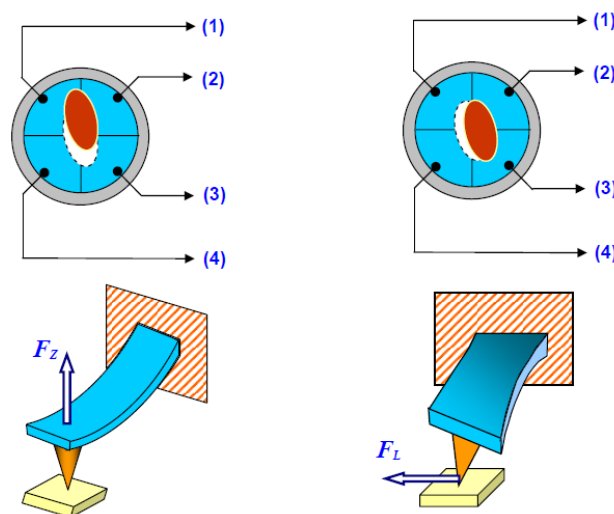


Figure 3. Schematic representation of four-segment PSD and dependence of the position of the laser spot on the deflection of the cantilever. Numbers 1, 2, 3 and 4 indicate the sections of PSD (Mironov, 2004).

The interaction forces of the probe with the surface can be described using the Lennard-Jones potential curve. This dependence is shown in Figure 4. At small distances, repulsive forces prevail, while at larger distances the main role is played by the forces of attraction. The interaction potential is described by the Equation (2.1), where the first term is responsible for the repulsive forces at small distances. The second term is responsible for the long-range attraction caused by the dipole-dipole interaction (Van der Waals forces) (Seo and Jhe, 2008).

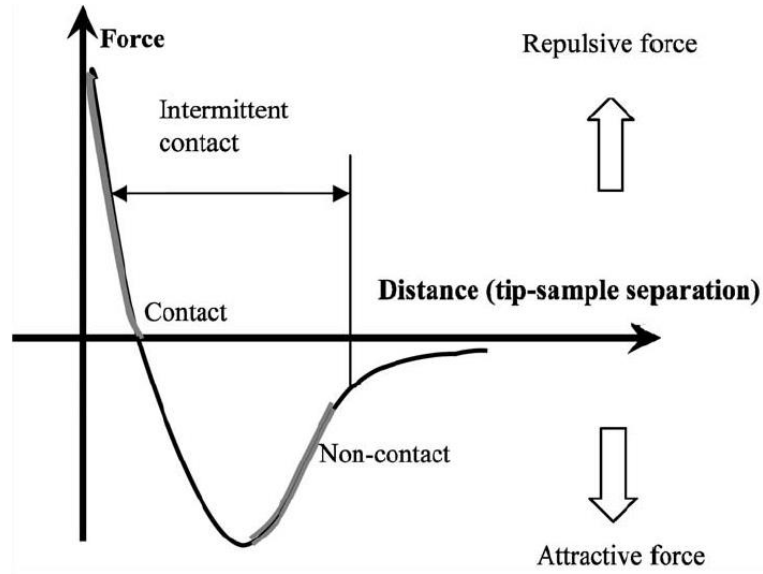


Figure 4. Lennard-Jones Potential (Jalili and Laxminarayana, 2004).

$$U(r) = 4\varepsilon \left[ \left( \frac{\sigma}{r} \right)^{12} - \left( \frac{\sigma}{r} \right)^6 \right], \quad (2.1)$$

where  $\varepsilon$  is depth of the potential well,  $\sigma$  is the distance where energy of interaction becomes zero, and  $r$  is the distance between particles.

### 2.1.1. Basic components of an AFM

The basic components of an atomic force microscope are laser, cantilever and probe, scanner, photodiode, and feedback loop system. The AFM scanner is made of piezoelectric material. Its main feature is the ability to change its size when an electric field is applied. The most widespread are tube-shaped scanners. A schematic representation of such a scanner

is shown in Figure 5. The piezoelectric tube consists of several independent electrodes that allow changing the position of the scanner in three directions X, Y, Z. Thus, supplying voltage of opposite signs to external opposite electrodes (i.e. X, -X or Y, -Y) leads to the tube bending in the given direction, which allows changing the scanner's position in the X and Y planes, respectively. The inner electrode is responsible for the scanner's height. It is changed by compressing and stretching along the Z axis. The size of the scanned area depends on the height and diameter of the piezoelectric tube. Typical lateral scanning resolution is from tens of angstroms to hundreds of microns, while the height can vary in the range from sub-angstroms to 10 microns (Cardellach i Redon, 2013).

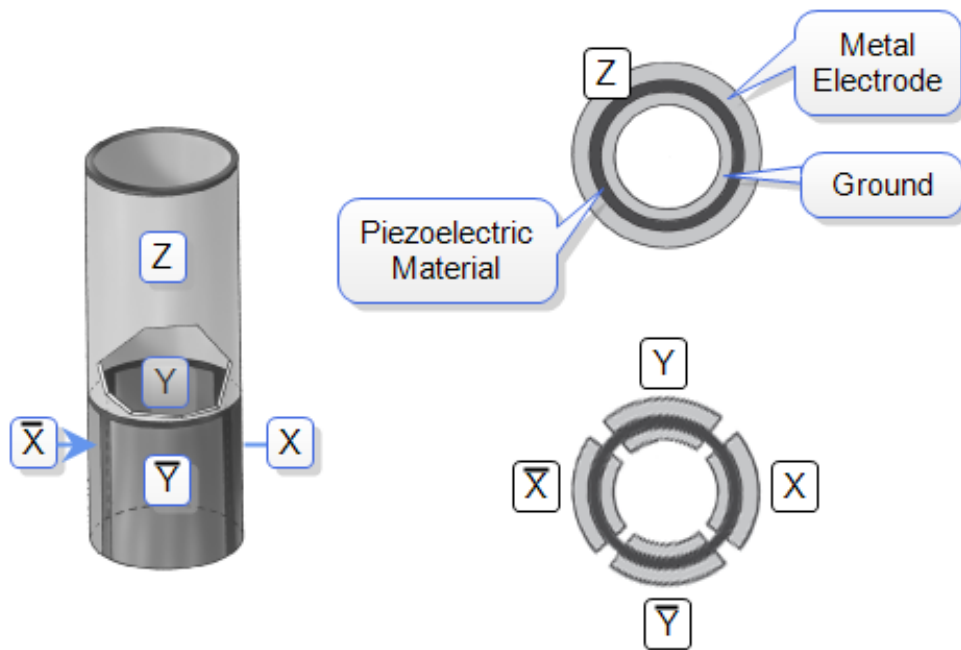


Figure 5. Schematic representation of the tube-shaped piezo scanner.  $\bar{X}$ ,  $\bar{Y}$  are the opposite electrodes to X and Y electrodes, respectively (*Piezoelectric Scanners*, no date).

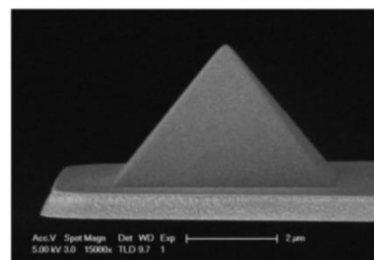
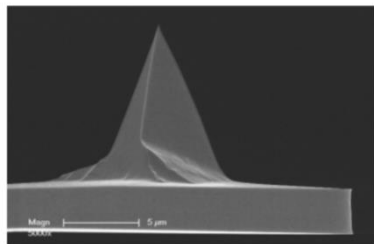
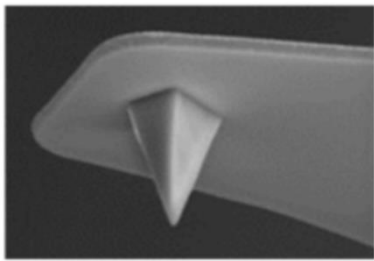
Second important element of the AFM is the probe, the image of which is shown in Figure 6. The probe is a sharp tip fixed to a cantilever. The probe geometry and its radius affects the lateral resolution. A cantilever is an elastic console that can have different geometric variations. It can be also made of different materials, which determines its mechanical and dynamic properties. One of the main parameters of the cantilever is its spring constant, which determines the force of interaction of the probe with the surface. The force of interaction can be expressed by Hooke's law:

$$F = -kx, \quad (2.2)$$

where  $k$  is the spring constant of the cantilever and  $x$  is the cantilever displacement from its normal position.

Silicon Si and silicon nitride  $\text{Si}_3\text{N}_4$  are most often used for the probes manufacturing. They can also have additional coatings such as gold, aluminum or platinum to obtain various properties necessary for performing a particular type of analysis, for example, to study magnetic properties (cobalt-chrome CoCr coating) or to measure current (platinum-iridium Pt-Ir coating).

### Tip Specification



### Cantilever Specification

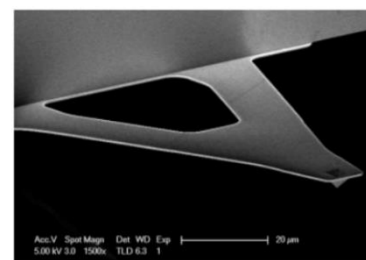
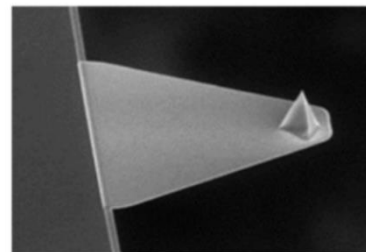
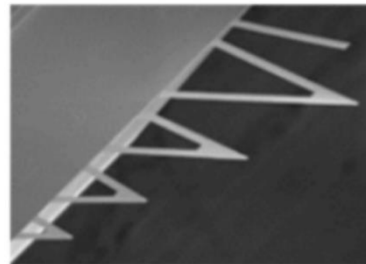


Figure 6. Scheme of tips and cantilevers shapes from Bruker (*Probes - Bruker AFM Probes*, no date).

The feedback loop system of an AFM monitors cantilever deflection and amplitude changes. While comparing the input signal with the output signal, the feedback loop system controls the Z-position of the scanner by changing the applied voltage to the electrode. This allows keeping the interaction force between the probe with the surface constant. Thus, the resulting

“image” represents the feedback voltage, which was applied to the electrode. The feedback loop of an AFM is represented in Figure 7. The key parameters of the system are setpoint, error signal and gain. The *setpoint* is the operator-set value of the deflection or amplitude, which is kept constant. The *error signal* is the difference between the operator-set setpoint and the real value that was measured. How quickly the system reacts to an error signal depends on the *gain* value. However, it is worth noting that if the gain is set too high, the feedback loop can react to even small interference, thereby causing noise in the image.

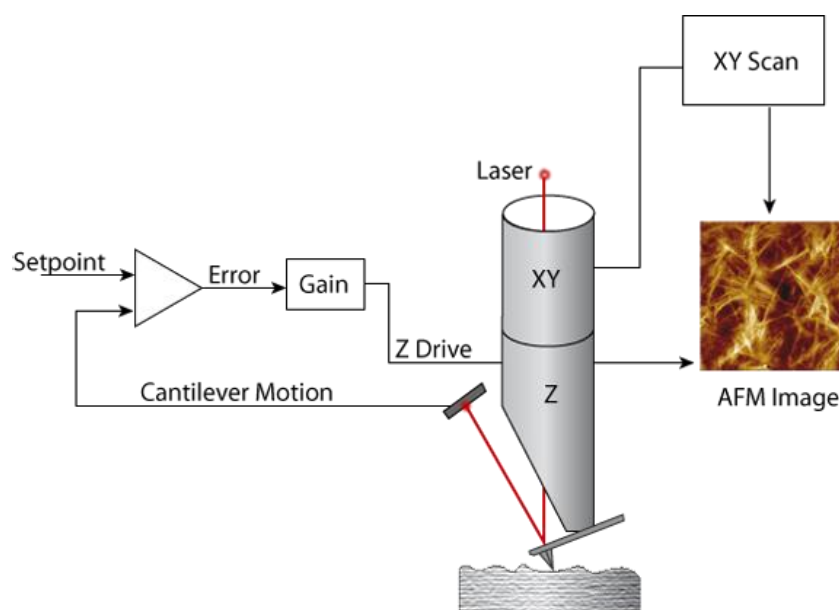


Figure 7. Schematic representation of the feedback loop system of an AFM (*Z Feedback Loop*, no date).

### 2.1.2. Modes of operation of an AFM

In AFM are three main modes of operation: contact, semi-contact and non-contact.

In *contact mode*, the probe directly touches the sample surface. The cantilever's bending reflects the repulsive force from the sample surface. Two scanning methods can be distinguished: constant height method (constant average distance between the base of the probe and the surface of the sample) and constant force method. In the first method, the cantilever is positioned at a constant height from the surface and its bend characterizes the topography. In the constant force method, the deflection of the cantilever is constant and is

supported by a feedback system, while the height changes, which allows understanding of the sample relief (Marrese, Guarino and Ambrosio, 2017).

Contact mode allows investigation of solid surfaces. Usually cantilevers with a low stiffness coefficient are used as a probe. The main disadvantage of this method is the possibility of surface damage due to straight contact between the probe and the sample.

The *non-contact mode* was invented in 1987, a year after the contact mode (Martin, Williams and Wickramasinghe, 1987). In the non-contact mode, the probe is located at small distance from the sample surface, and it oscillates at a frequency close to its resonance. A force acts on the probe from the surface, and the force changes with distance. The main contribution is made by van der Waals interaction. A change in the interaction force leads to a shift in the amplitude-frequency and phase-frequency characteristics of cantilever. The surface relief can be determined by the shift's magnitude. The advantage of this method is the ability to carry out measurements without damaging the sample surface.

Next mode is *semi-contact mode*. It has two working modes: tapping and Peak Force. Also in the *tapping mode*, the cantilever oscillates at a resonant frequency above the surface with an amplitude of 10 - 100 nm (Etzler and Drelich, 2012). However, in contrast to the non-contact mode, the probe still touches the sample slightly in the lower half-period. Changing the amplitude of the probe oscillation allows investigation of the surface topography. This method is the most versatile of all AFM methods. It damages the sample less, but on the other hand, it takes longer to measure the sample.

Second regime of the semi-contact mode is *Peak Force Tapping*. This mode is very similar to tapping mode in that the cantilever also oscillates and touches the specimen lightly. However, in contrast to the previous mode, oscillatory movements are performed at a frequency less than the resonant frequency, due to which it is possible to avoid the filtering effect and the dynamics of a resonating system. Thus, Peak Force Tapping combines the advantages of contact and semi-contact modes, namely, direct force control and avoidance of damaging lateral forces (Kaemmer, 2011). Additional mode is *Peak Force Quantitative Nanomechanical Mapping*. This mode allows less damage to the probe by controlling peak normal force and minimizing lateral forces acting on the probe. The mode also allows to measure surface properties. For example, elastic modulus, adhesion, deformation, dissipation (Young *et al.*, 2011; *PeakForce QNM*, no date).

## 2.2. Kelvin Probe Force Microscopy

Kelvin Probe Force Microscopy (KPFM) is most often a two-pass technique. Using this method, the first pass investigates the surface topography, and the second pass measures the contact potential difference between the sample and the AFM conductive probe (Nonnenmacher, O'Boyle and Wickramasinghe, 1991). The relief's investigation is carried out in a Peak Force Tapping mode, and then the probe rises above the sample at a certain distance above the surface, which is set by the operator. A voltage is applied to the probe while the probe is repeating its relief, and the work function of the sample surface is measured. The work function is the minimum energy required to remove an electron from the surface of a solid in a vacuum.

The AC voltage applied to the probe during the second pass causes the cantilever to vibrate. If the surface potential does not coincide with the applied potential, then the force arising between the tip and the surface leads to additional oscillations of the cantilever. The feedback system supplies a constant voltage to compensate for the potential difference between the probe and the surface. The total voltage applied to the probe can be expressed by following equation (2.3):

$$V_{tip} = V_{dc} + V_{ac} \sin(\omega t), \quad (2.3)$$

where  $V_{dc}$  and  $V_{ac}$  are the supplied DC and AC voltage, respectively (Melitz *et al.*, 2011).

Resultant capacitive force between probe and surface is given by the equation (2.4):

$$F_{cap} = \frac{1}{2} (V_{tip} - \phi(x))^2 \frac{\partial C(z)}{\partial z}, \quad (2.4)$$

where  $\phi(x)$  is the surface potential and  $C(z)$  is the capacitance of the probe-sample system.

The force acting from the side of the sample and leading to additional oscillations of the cantilever is described by equation (2.5).

$$F_{cap-\omega} = \frac{\partial C(z)}{\partial z} (V_{dc} - \phi(x) V_{ac}) \sin(\omega t). \quad (2.5)$$

Thus, the feedback loop supplies a constant voltage  $V_{dc}$  so that  $\omega$  becomes zero and  $V_{dc}$  becomes  $\phi(x)$ . The value of the potential  $V_{dc}$  then reflects the distribution of the surface

potential. Figure 8 shows the energy diagram of the probe-sample system, where  $\phi_s$  and  $\phi_t$  correspond to the work function of the sample and the probe, respectively.

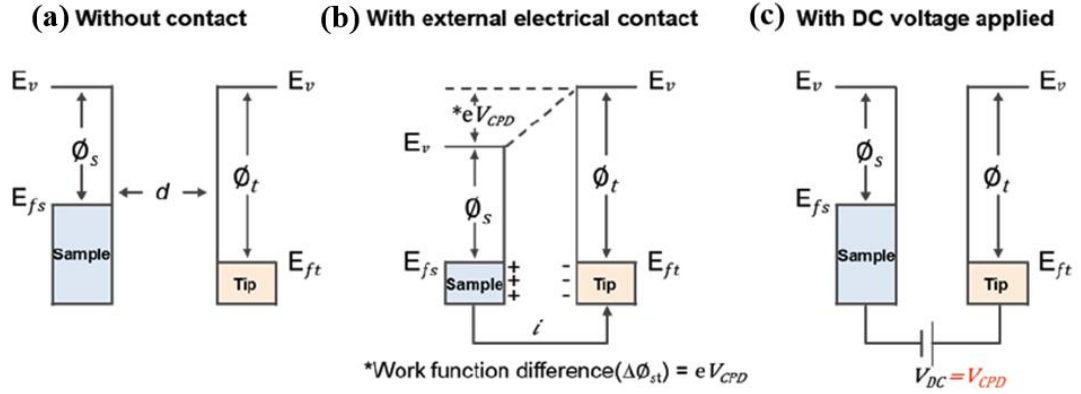


Figure 8. Energy diagram of the probe-sample system.

(a) the sample and the probe are located at a distance  $d$  and are not electrically connected;  
 (b) the sample and the probe are electrically connected, the Fermi levels are equalized due to the current  $i$ , the contact potential difference  $V_{CPD}$  appears; (c) a constant voltage  $V_{DC}$  is applied, thereby compensating for  $V_{CPD}$  (*Kelvin Probe Force Microscopy (KPFM)*, no date).

## 2.3. The physical concept of converting humidity to electricity

- *Protein nanowires produced by Geobacters*

The investigation of scientists from University of Massachusetts Amherst is a recent achievement in the conversion of air humidity into electricity. They have developed a device capable of generating energy from air (Liu *et al.*, 2020). The device is based on microbes *Geobacter sulfurreducens*, which produce conductive protein nanowires. The microbes were discovered more than 30 years ago (Lovley *et al.*, 2011). They are capable to obtain energy by oxidizing organic compounds and metals.

A film consisting of nanowires produced by *Geobacters*, about 7 microns thick, is placed between gold electrodes deposited on glass (Figure 9). Protein nanowires are heterogeneous in diameter, which leads to a porous structure, which in turn facilitates the transmission of water and, accordingly, the moisture gradient inside the structure. The moisture gradient explains the generation of voltage within the film. Carboxyl groups located on the surface of nanowires are a source of mobile protons. The concentration gradient of protons leads to their diffusion, due to which an electric field arises.

The device generates a voltage of about 0.5 V, while the short-circuit current is 250 nA. During 20 hours of work through the load resistor, the voltage drops to 0.35 V. However, within 5 hours the voltage is restored to a 0.5 V (Figure 10). The device maintained a constant voltage at the level of 0.4 – 0.6 V, during 2 months of its monitoring. Serial connection of 17 devices made it possible to generate a voltage of 10 V.

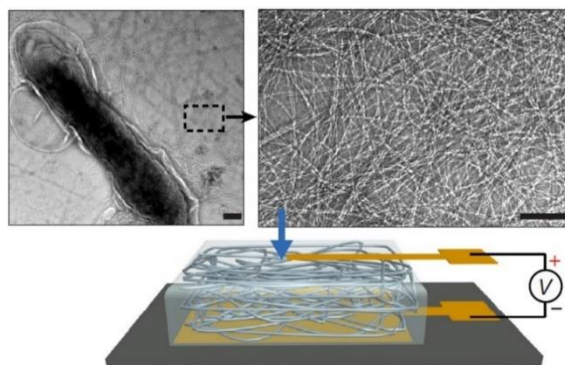


Figure 9. TEM images of bacteria *Geobacter sulfurreducens* (upper left) and purified nanowire network (right corner), schematic representation of the device (lower figure) (Liu *et al.*, 2020).

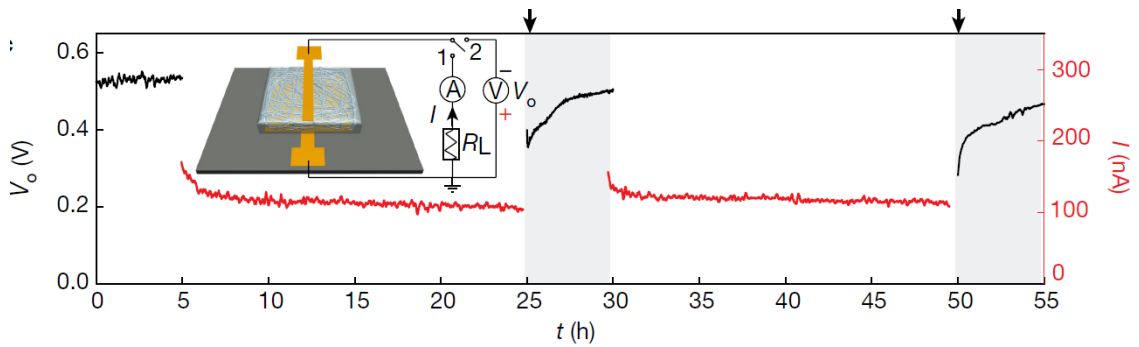


Figure 10. Generated voltage (black) and current (red) versus time (Liu *et al.*, 2020).

- *Zirconia nanoparticles*

Second mechanism for generating electricity is the “direct conversion of the water adsorption energy to electricity on the surface of zirconia nanoparticles” proposed by Doroshkevich *et al.*, 2019. The method is based on chemo-electronic conversion. When an electrically neutral water molecule comes into contact with an electrically neutral surface, dissociative absorption occurs. A negative charge appears on the surface, comparable to the volume of a nanoparticle, which leads to a bending of the energy band in the near-surface region, and the electron density shifts towards the adsorbed layer (Figure 11).

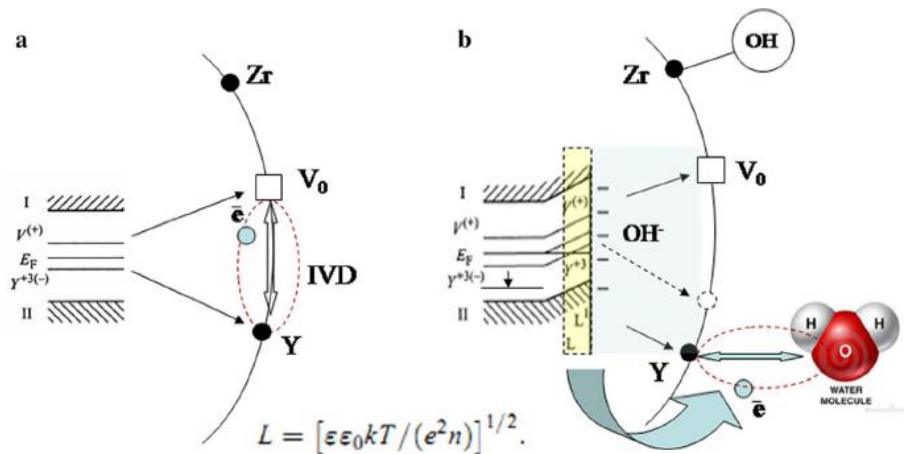


Figure 11. Schematic representation of the adsorption mechanism of electron emission.

(a) initial state of the system; (b) system after adsorption of water molecules

(Doroshkevich *et al.*, 2019).

Dissociative absorption is a process during which ions are partially in a free state and, in the presence of an electric field gradient, able to transfer charges to the electrodes. This leads to

a change in the length of the interaction between the oxygen vacancy and the impurity ion. Thus, the influence of the alloying element weakens and the crystal structure in the subsurface volume becomes monoclinic, which is characteristic of zirconium dioxide  $ZrO_2$  at room temperature. The absorption mechanism of the tetragonal-monoclinic phase (T-M) transformation is shown in Figure 12.

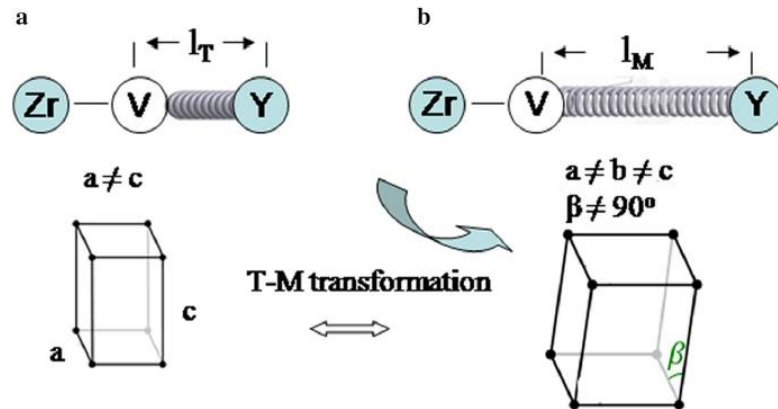


Figure 12. Schematic representation of the adsorption mechanism of the T–M transformation. (a) initial state of the system; (b) system after adsorption of water molecules (Doroshkevich *et al.*, 2019).

A chemo-electronic converter is shown in Figure 13 (a). Its size is 35x20 mm. The deposited film has a porous structure, which allows water molecules to penetrate into the sample and interact with the  $ZrO_2$ -based material. The time dependence of the potential of a sample placed in an atmosphere with a 99% RH is shown in Figure 13 (b). It can be seen that absorption first leads to an increase in the electric potential difference to 80 mV, and then to a decrease to 0 V.

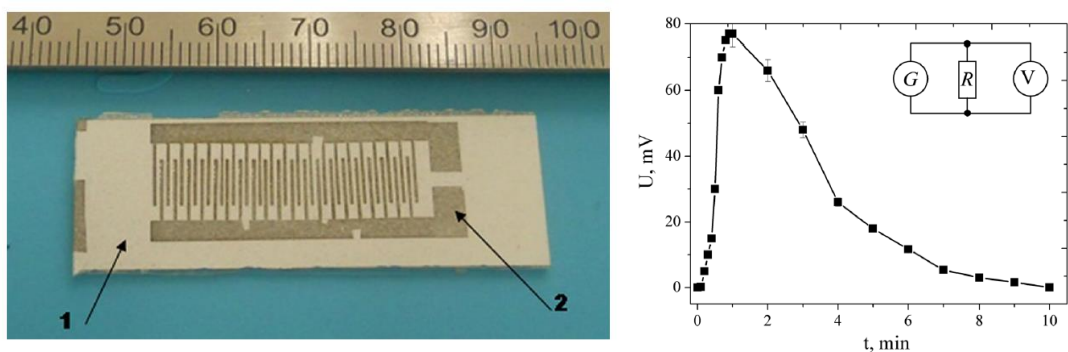
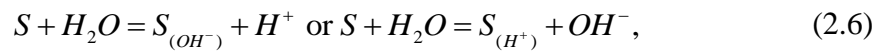


Figure 13. (a) a chemo-electronic converter, where 1 is a functional layer deposited on glass and 2 is an interdigital contact structure. (b) Dependence of the sample electric potential on time at a RH of 99% (Doroshkevich *et al.*, 2019).

- *Charge accumulation on metals*

Third principle of charge accumulation on metals with a change in the RH of the air was presented in the work of Ducati, Simões and Galembeck, 2010b. In the course of the work, it was shown that isolated metals inside a Faraday cage accumulate a charge when the air humidity is above 50%. The mechanism of charge accumulation is explained by the fact that water molecules adsorbed from the air transfer an excess charge to an isolated metal with an oxide coating, contributing  $H^+$  or  $OH^-$  ions onto its surface. What kind of charge will be formed on the surface depends on the contributed ion. The type of ion contributed, in turn, depends on the type of oxide coating. Thus, alumina accumulates a negative charge by binding to the hydroxyl ion  $OH^-$ , while chromium oxide binds to the hydrogen ion  $H^+$ , acquiring a positive charge. A schematic process of charge formation is shown in Figure 14. Thus, the process of charging a metal with a change in RH is one more simultaneously occurring acid-base reactions, which can be described as follows:



where  $S$  is surface sites,  $H^+$  and  $OH^-$  are ions released into the atmosphere, which bind to clusters of desorbed water molecules.

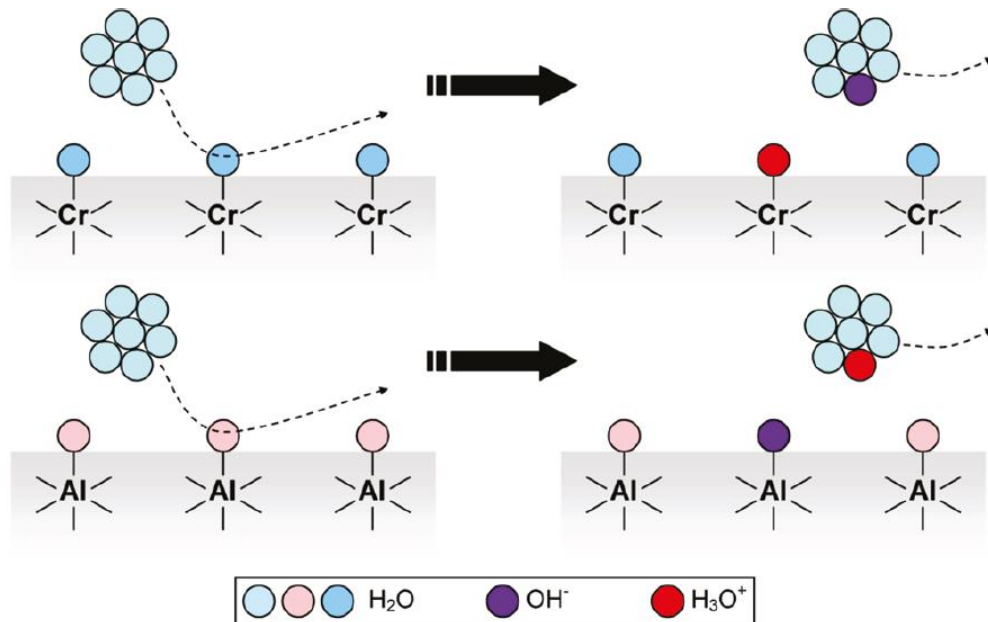


Figure 14. The mechanism of transfer of positive (upper figure) and negative (lower figure) charges from the atmosphere to a metal surface (Ducati, Simões and Galembeck, 2010b).

In the work, a simple device was developed, which is a capacitor made of folded sheets of filter paper, aluminum, filter paper, stainless steel, and filter paper. On both sides, metal electrodes coated with oxides of different adsorption capacity, separated by a porous dielectric with a high capacity to absorb water vapor, were connected. The device was placed in a grounded aluminum casing that was placed in a Faraday cage. The measurement results are represented in Figure 15 from which it is visible that the voltage increases with RH increasing. It flattens out with charged electrodes and dissipates when the electrodes are short-circuited. It should be noted that the experiment is well reproducible.

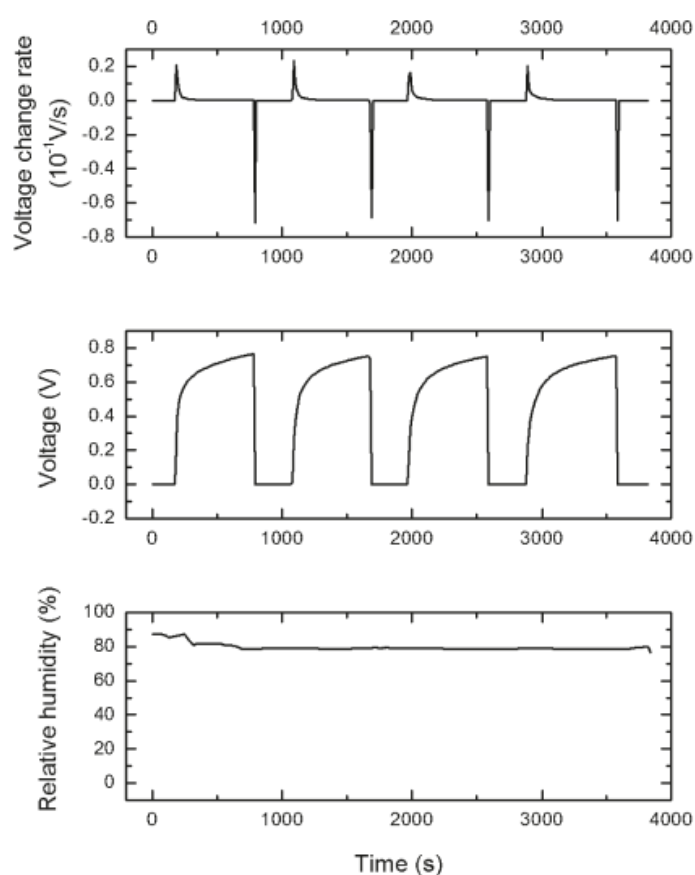


Figure 15. Cycles of charging and discharging an experimental capacitor (Ducati, Simões and Galembeck, 2010b).

- *Films of noncrystalline silica and aluminum phosphate particles*

One more study devoted to the change in electric potential with changes in the RH of the air is presented in the work of Gouveia and Galembeck, 2009. The work investigated noncrystalline silica and aluminum phosphate particles films using KPFM. It was shown that

the value of the potential increases with increasing RH and decreases with decreasing RH (Figure 16). In this case, the potential of the sample always remains negative. The authors explained this result by the process of ion separation simultaneously with the acts of adsorption-desorption. Desorbed water molecules carry an excess positive charge while the sample potential is negative, that is, the particles carry an excess negative charge. This indicates specific interactions between water ions and aluminum phosphate ions in the sample.

A similar experiment was performed using Stöber silica particles. Also, these measurement results showed the relationship between the potential and the value of the RH of the air. However, the dependence is reversed with respect to previous case, as with an increase in relative humidity, the value of the film potential decreases (Figure 17). It should also be noted that a change in moisture content leads to irreversible structural changes in the samples, although the experiments have good repeatability. In addition, the reversibility of the experiment for the sample with Stöber silica particles is higher than for the sample with aluminum phosphate particles.

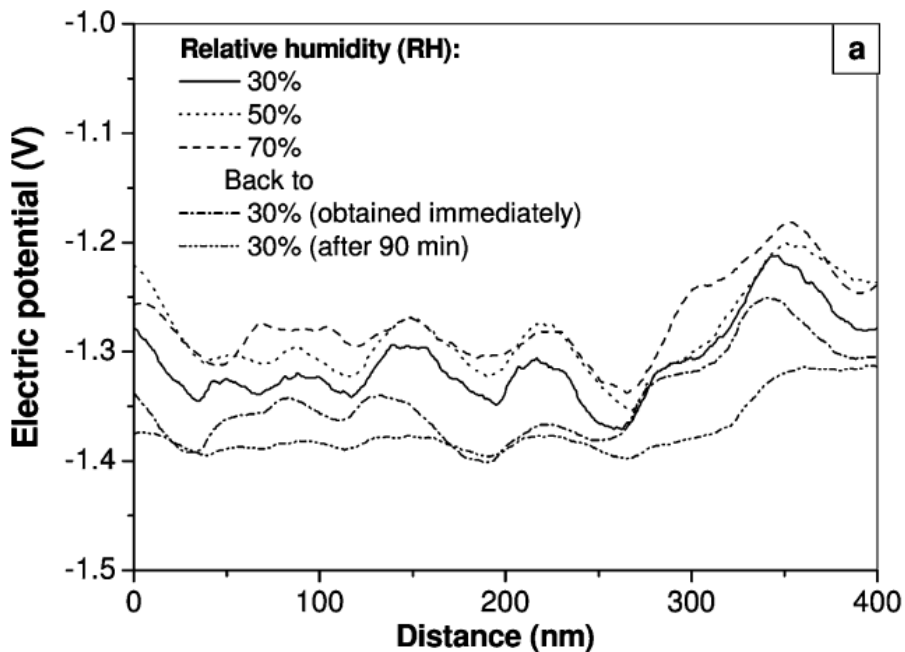


Figure 16. Results of measuring the electric potential of a sample with aluminum phosphate particles at different values of RH (Gouveia and Galembeck, 2009).

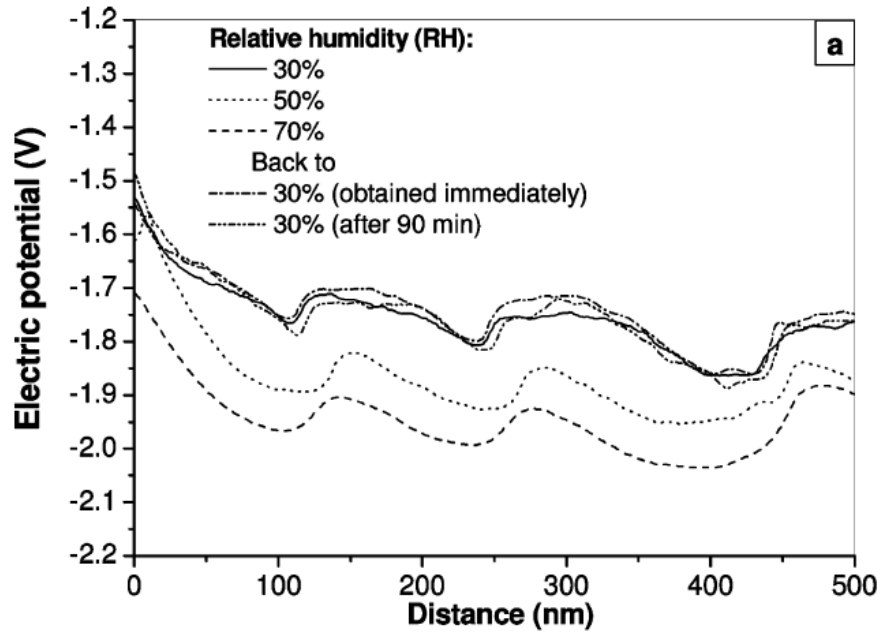


Figure 17. Results of measuring the electric potential of a sample with Stöber silica particles at different values of RH (Gouveia and Galembeck, 2009).

## 2.4. Related works

Among the earlier completed works on this topic, two master's theses can be distinguished. The first is "Effect of humidity on electric potential of  $ZrO_2$  nanocomposite investigated by AFM / KPFM" by Anum Rasheed (Rasheed, 2017). The second is "Humidity to electricity converter based on zirconia nano-particles" by Nafiseh Mohammadi (Mohammadi, 2017). Anum Rasheed investigated zirconium-based nanocomposites. The sample under study was placed in a gas cell of an AFM, in which the RH varied in the range from 0% to 100%. The KPFM was used to measure the potential on the film surface. A direct correlation between the RH of the air and the potential of the film was found. The measurement results is shown in Figure 18. From the figure it can be seen that the potential value increases with increasing humidity in the gas cell. It should be noted that the potential variation range was  $\sim 500$  mV, which is suitable for devices with low power consumption. The potential channel is shown in Figure 19. It is visible that the images have streaks that corresponds to the noise.

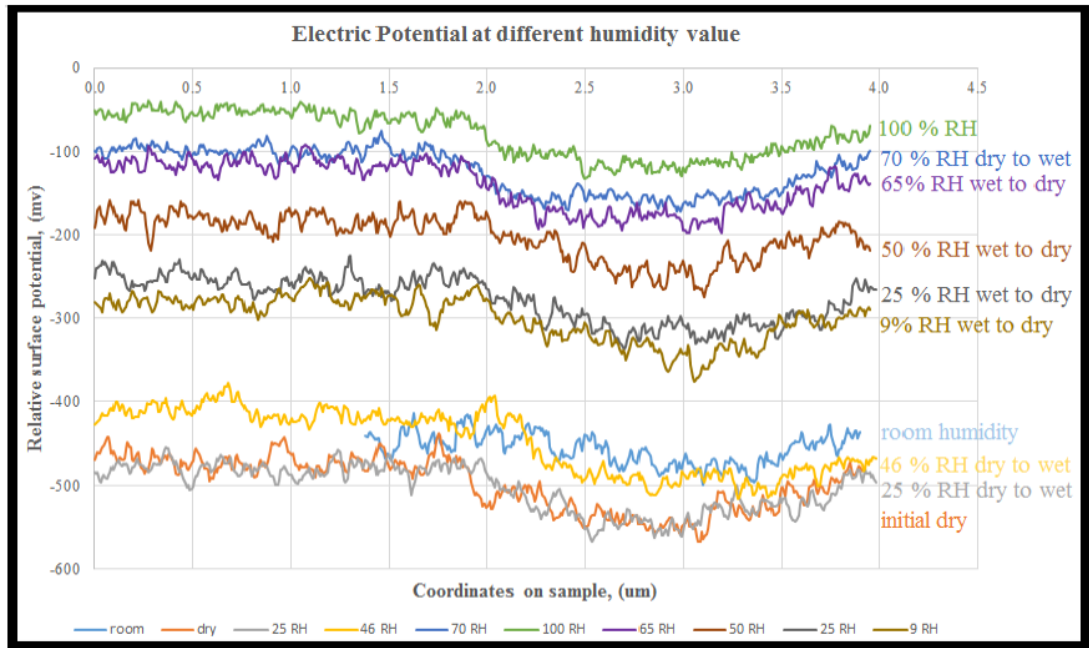


Figure 18. Comparison of electric potential for different RH values (Rasheed, 2017).

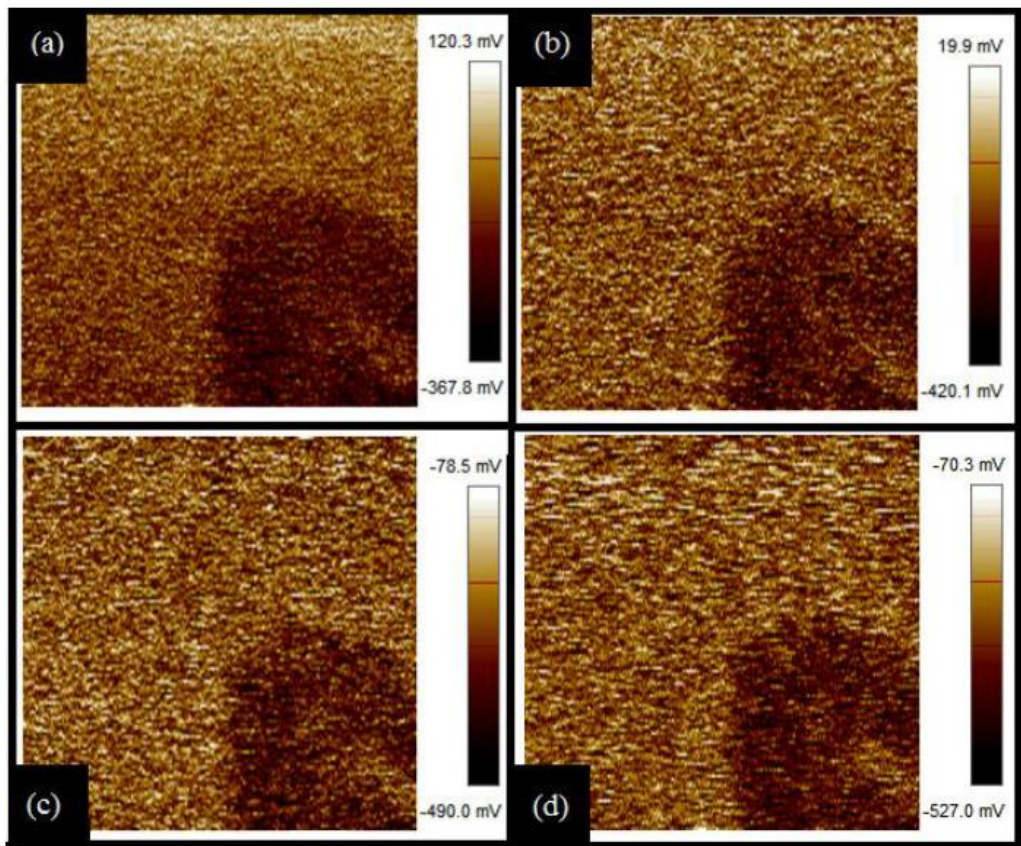


Figure 19. Potential map for different RH: (a) dry air, (b) 25%, (c) 50%, (d) 70% (Rasheed, 2017).

In the work of Nafiseh Mohammadi, nanocomposites based on zirconium oxide were investigated in more detail. The composites had different concentrations of ZnO<sub>2</sub> nanoparticles and it was found that samples with a 50% concentration produce the highest potential value. The dependence of the film potential on the relative humidity was revealed as in the Rasheed work. However, direct correlation between an increase in the potential value with an increase in relative humidity was not observed. The research results are shown in Figure 20.

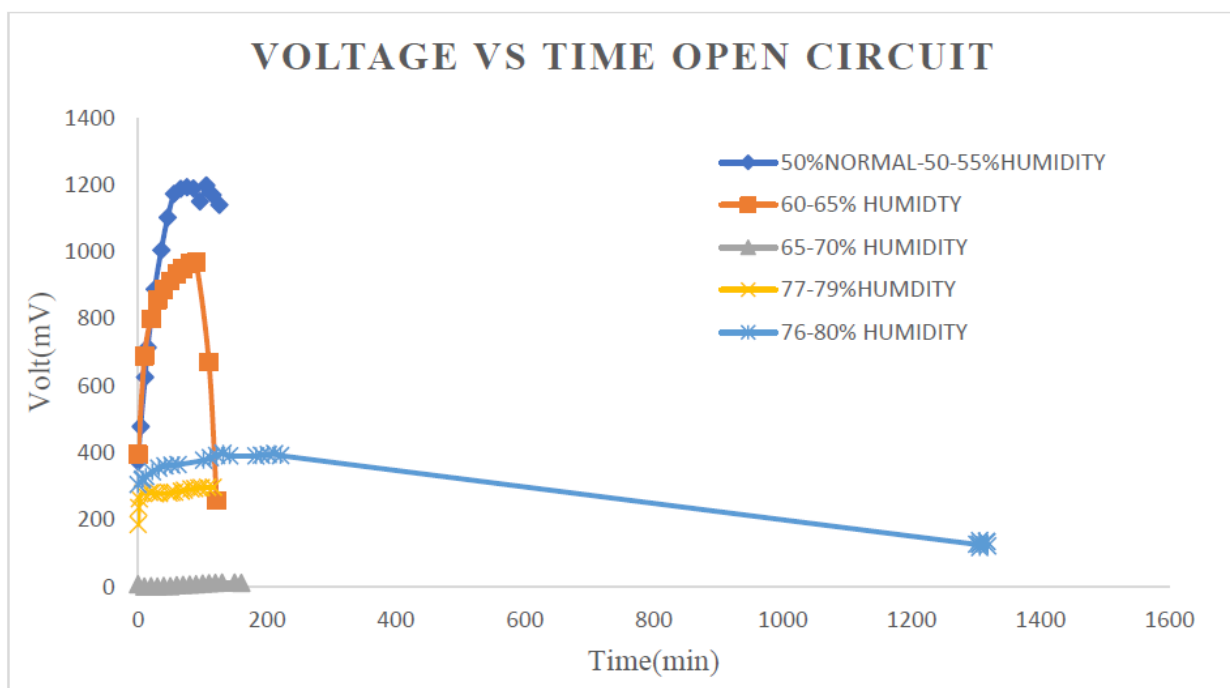


Figure 20. Voltage in open circuit for different relative humidity values (Mohammadi, 2017).

In the work of Adamchuck *et al.*, 2020, the influence of water vapor adsorption and desorption on the surface of tin dioxide SnO<sub>2-δ</sub> based films on their conductivity was investigated. It was shown that films with higher conductivity are more sensitive to changes in RH than films with lower conductivity. The percentage change in resistance with humidity over time is represented in Figure 21. It can be seen that conductivity is increasing below 30% RH and decreasing above 30% RH. This dependence is caused by dissociative adsorption of water molecules with the formation of hydroxyl groups.

The authors explain the use of tin dioxide by the fact that, due to its non-stoichiometry, oxygen is easily adsorbed on its surface. This leads to the fact that tin dioxide has a high surface reactivity with reducing and oxidizing gases. In addition, oxygen vacancies are

electron donors in SnO<sub>2</sub>, due to which high conductivity is ensured (Davydov, Moshnikov and Fedotov, 2006; Yuliarto, Gumilar and Septiani, 2015).

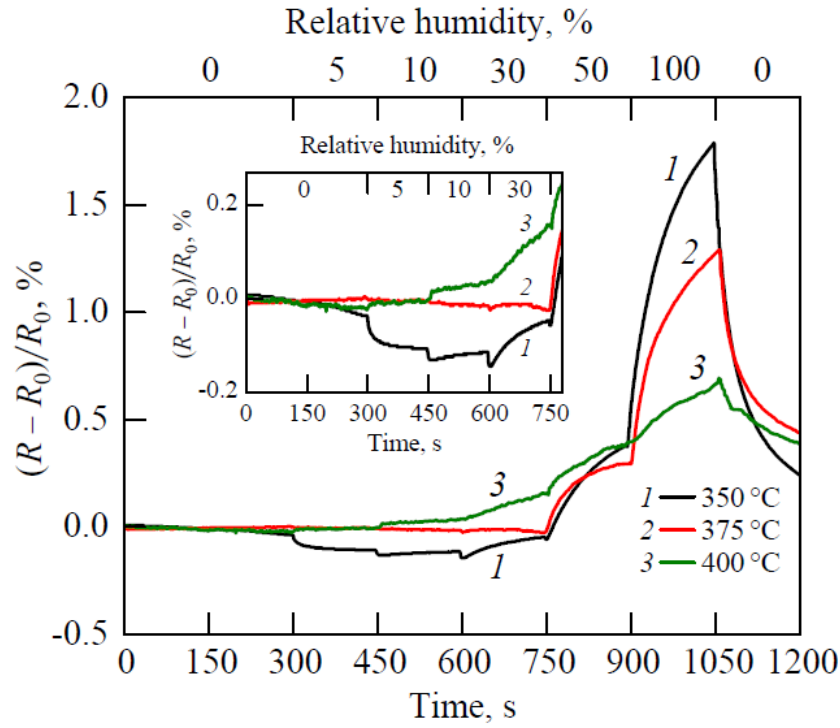


Figure 21. Change in the resistance of films synthesized at various annealing temperatures in the second stage of annealing (1: 350 °C; 2: 375 °C; 3: 400 °C) with changes in RH (Adamchuck *et al.*, 2020).

Based on earlier research, the following main points can be distinguished. Materials based on zirconium oxide and materials based on tin dioxide were investigated. For materials based on zirconium nanoparticles, studies were carried out on the effect of changes in RH on the electric potential value. It was found that changes in the magnitude of the potential occur, however, no clear correlation was found between these two parameters. The results of studying films based on tin dioxide showed the dependence of the change in RH on the films resistance. In earlier works, the issue of experiments repeatability also remained unexplored. Thus, to carry out measurements within the framework of this master's thesis, samples based on tin dioxide, investigated in the work of Adamchuck *et al.*, 2020, and the installation for changing the humidity used in the work of Rasheed, 2017 were chosen.

### 3. Measurement procedure

#### 3.1. NanoScope Software

##### 3.1.1. Measurements in Nanoscope software

Measurements are made in PeakForce Kelvin Probe Force Microscopy.

The first step is probe installation and laser setting. The laser is adjusted in such a way that its parameters have following values: vertical “*vert*” and horizontal “*horz*” photodetector position should be zeroes or at least less than 0.1, and the value of intensity “*sum*” should be in a range 4.5 – 7 (Figure 22). Optical microscope allows to monitor where the laser beam hits (Figure 23).



Figure 22. Parameters of the adjusted laser.

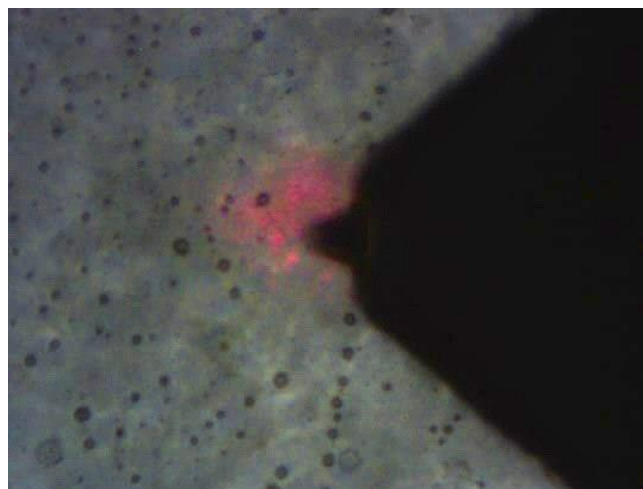


Figure 23. The probe and laser beam in optical microscope.

The second step is the determination of cantilever's resonant frequency. This may be done by manual tuning with a tapping mode experiment (Figure 24). In a graph *drive frequency*, the resonant frequency provided by a cantilever's specification, should be written. Auto tuning will be done in a range from start to end frequencies, which are set by the operator (Figure 25).

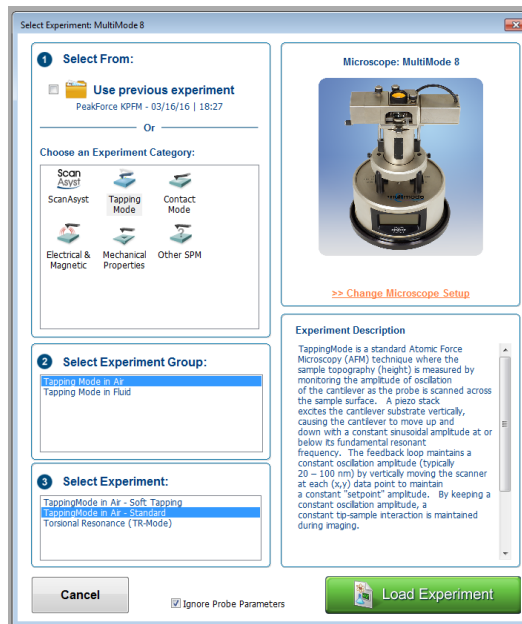


Figure 24. Experiment selection.

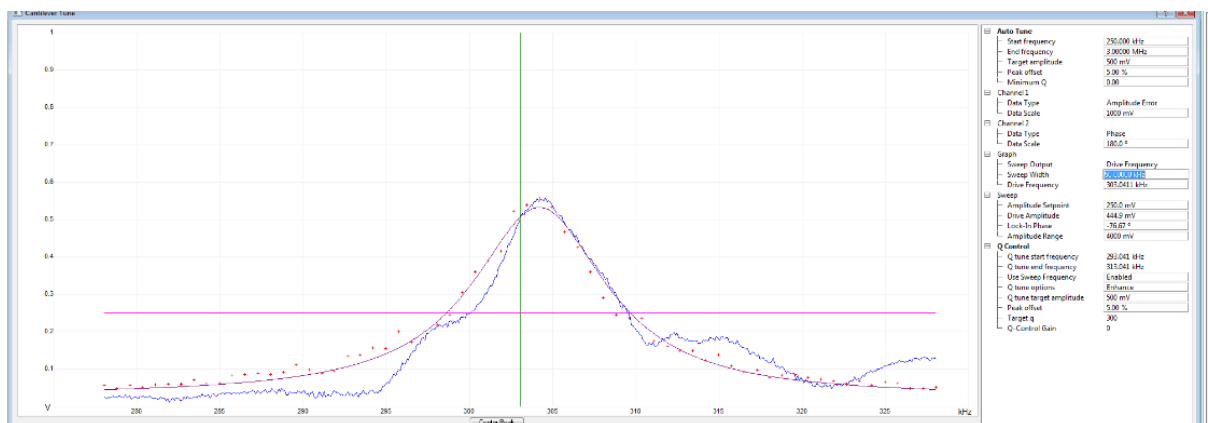


Figure 25. Tuning the resonant frequency.

The next stage is setting parameters of the PeakForce KPFM experiment. Setting is done at the *Expanded mode*. *Scan Size* and *Aspect Ratio* determine the area to be investigated. For engaging *Scan Size* is 10 nm. The size is increased during the scan. *X, Y offset* and *Scan Angle* determine from which point and in which direction the probe will move. *Tip Velocity* is automatically detected from the *Scan Rate*. *Scan Rate* is chosen by AFM operator.

*Sample/Line* and *Lines* are responsible for the scanning resolution. In the graph *Feedback* the *ScanAsyst Auto Control* is chosen “*Individual*” and *ScanAsyst Auto Setpoint* is “*off*”. It is done to keep the same force of the interaction probe-sample. *Setpoint* determines the value of the feedback loop. Additionally, the graph *Interleave* the *Interleave Mode* is “*Disabled*” for engaging in the graph *Interleave*. Scanning is changed to “*Lift*” after probe is engaged to the sample surface. *Lift Scan Height* determines the height to which the probe will be raised for the second pass. The settings window is shown in Figure 26.

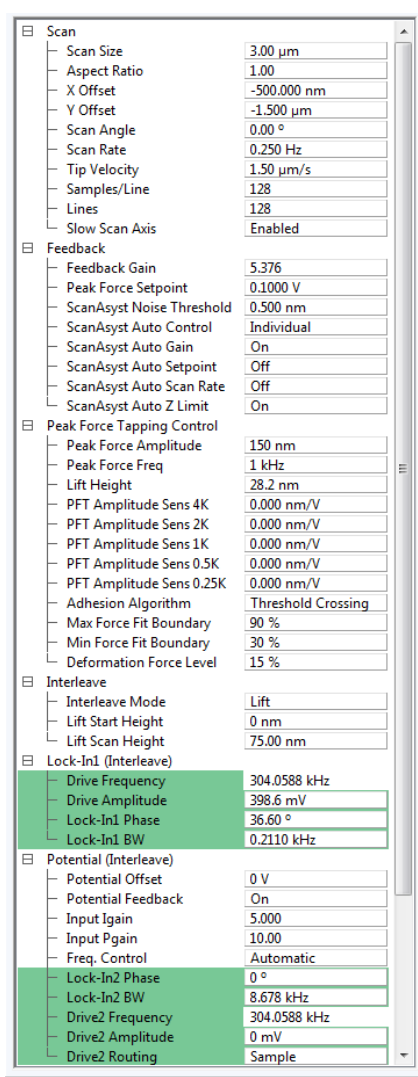


Figure 26. Setting the experiment parameters.

Probe may be engaged to the surface after setting parameters. *Force Monitor* is used for checking how probe landed (Figure 27). If probe landed well, red and blue lines at *Time-Force* dependence are almost equal and show the Lennard-Jones potential. The results are shown in the windows during the scanning of the sample. Different channels (up to

8 channels of different sample properties) may be chosen, e.g. height, peak force error, DMT modulus, logDMT modulus, adhesion, phase, potential and deformation (Figure 28).

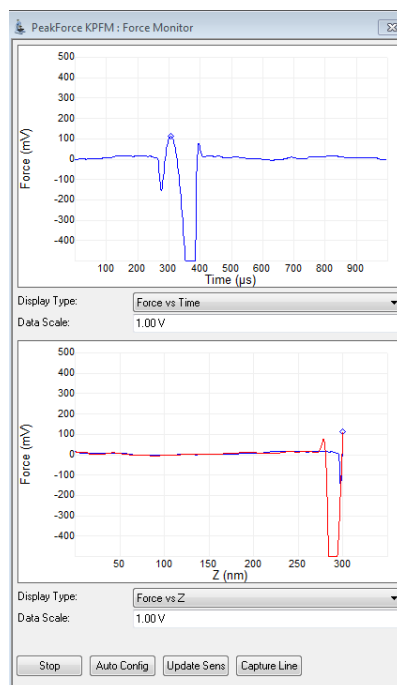


Figure 27. Force Monitor.

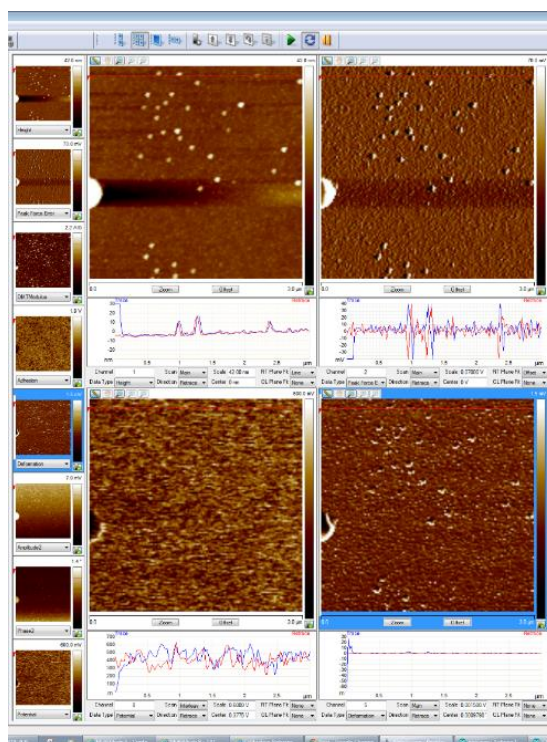


Figure 28. Displaying scan results.

### 3.1.2. NanoScope Analysis Software

The AFM images obtained during the experiments are processed by using the NanoScope Analysis v1.8 software provided by Bruker. The program for the filtering of images, removal of image artifacts, leveling of a relative slope of the surface, and qualitative and quantitative analyses. The workspace of the software is shown in Figure 29. On the left side there are information channels obtained during sample measurements. On the right side there is a window providing information about the selected channel as well as the scan parameters. There is a menu bar on the top and a toolbar just below it. The toolbar provides the following options for working with images:

- 2D and 3D visualization;
- Analysis: bearing, particle, power spectral density, depth, roughness, section, step and width;
- Tip qualification;
- Filtration: flatten, Gaussian, lowpass, median;
- Rotation, crop and split, image math.

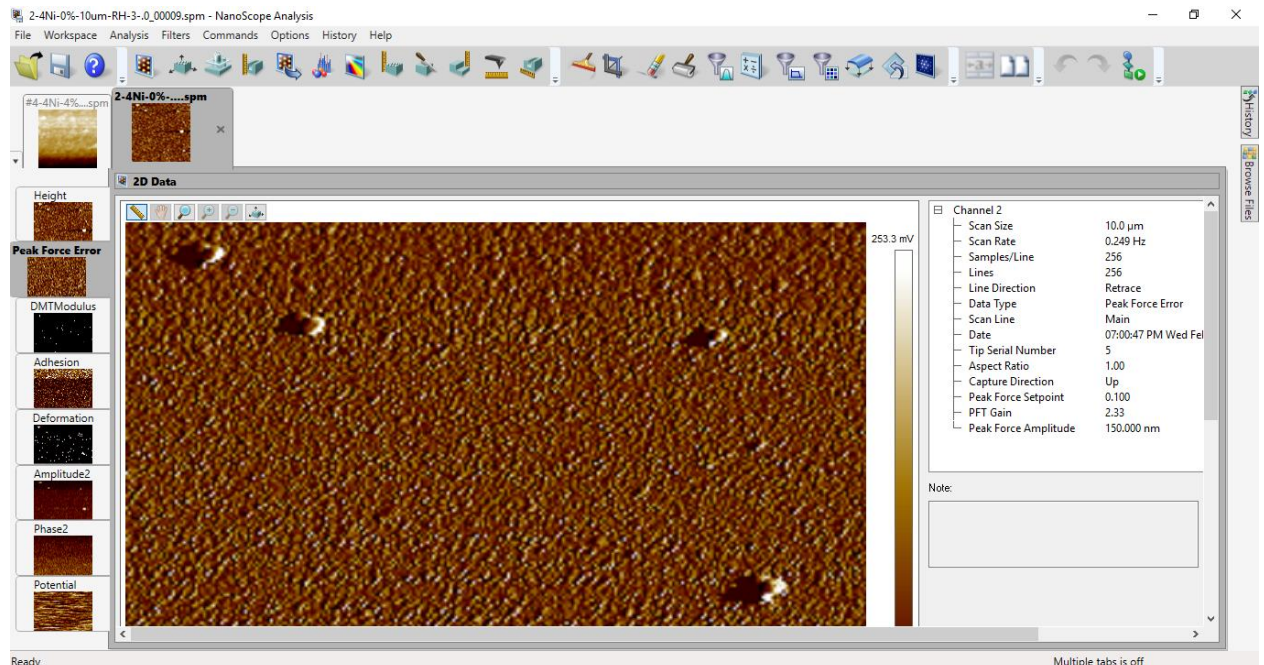


Figure 29. The workspace of NanoScope Analysis software.

Thus, the surface relief can be seen (Figure 30) in a volumetric version or its projection onto a plane with the help of visualization tools. The spatial characteristics of objects such as their

density and distribution can be evaluated by using analysis tools. Tip qualification evaluates the condition of the probe, that is, it analyzes how much the needle has evolved. Filtering tools smooth noisy image data, and the erase tool removes artifacts point by point, which further simplifies data analysis. Data processing makes data analysis easier, however, it must be very careful not to lose data due to over-processing.

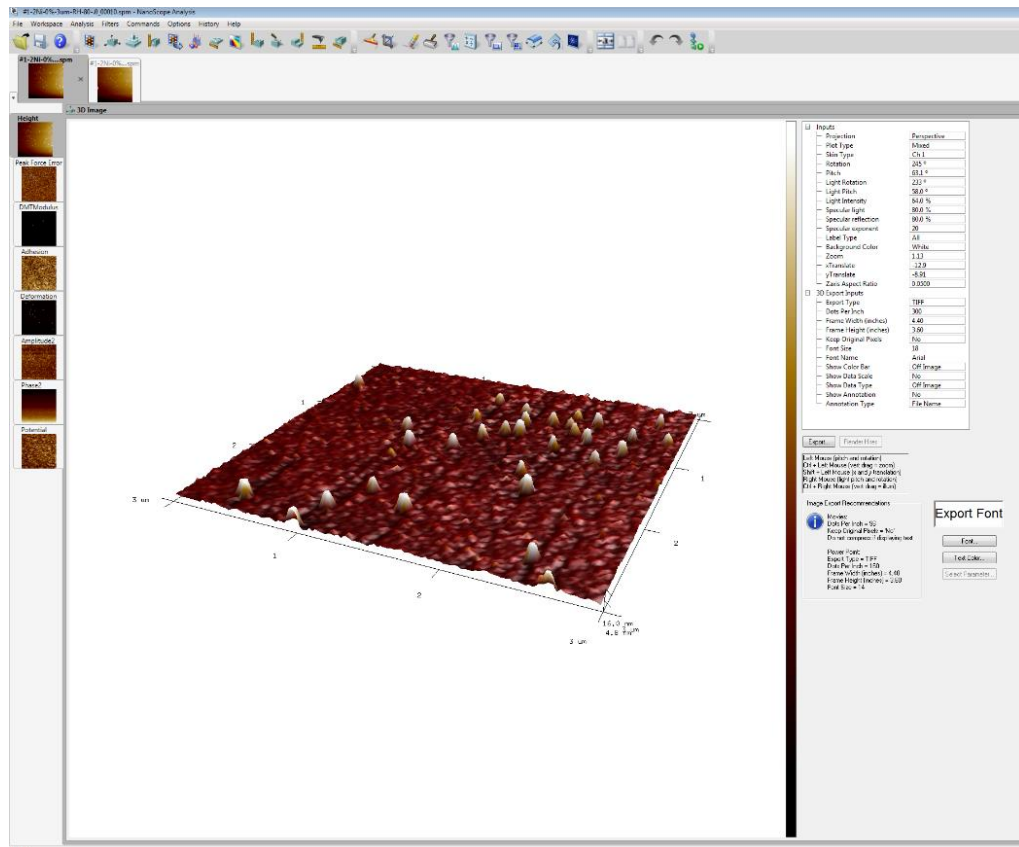


Figure 30. 3D visualization of the sample surface.

### 3.2. Equivalent electrical circuit of measurements

Equivalent electrical circuit of the measurement is shown in Figure 31. A metal wafer is placed on the piezo scanner, on which the sample is fixed. The sample is a tin-based conductive film that is deposited on a mica substrate. In order to create a contact between the metal substrate and the film, a silver conductive paste is used. The paste is applied to a metal substrate for fixing the sample on it. Also, a paste track is applied to the edge of the sample substrate, thereby electrically connecting the metal wafer and the tin film. During potential measurement, the conducting probe is located at a small distance from the sample surface and it makes oscillation movements.

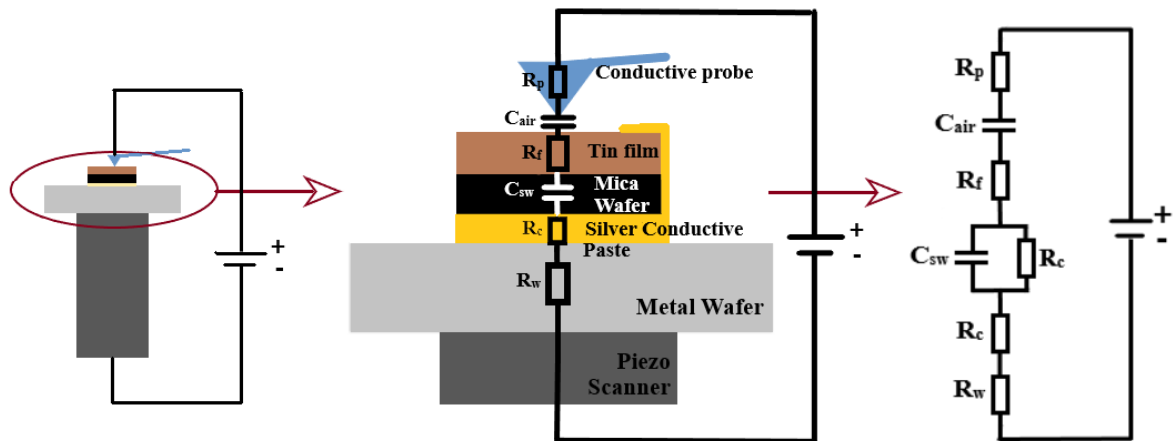


Figure 31. Equivalent electrical circuit of measurements.  $R_p$ : Probe Resistance,  $C_{air}$ : Air Capacitance,  $R_f$ : Tin Film Resistance,  $C_{sw}$ : Sample Wafer (Mica) Capacitance,  $R_c$ : Silver Conductive Paste Resistance,  $R_w$ : Metal Wafer Resistance.

### 3.3. Synthesis of tin dioxide films with clusters of ferromagnetic metals

The samples studied in this work are tin dioxide films doped with ferromagnetic metals. Synthesis and X-ray diffraction analysis were done in Belarus State University by V. Ksenevich. The synthesis of such films was performed by the method of magnetron sputtering in an argon plasma and reactive magnetron sputtering in an argon-oxygen plasma of a tin target (99.99 % purity) with nickel inserts followed by annealing in air. The oxygen content in argon-oxygen plasma with reactive magnetron sputtering varied in the range of 0 – 8 vol. %. The content of ferromagnetic metals in the films varied by changing the area of metal inserts in a tin target. The target diameter was ~ 10 cm. One or two nickel strips of 2 mm wide were used as ferromagnetic inserts to the target during deposition. Annealing in air after deposition was carried out in two stages: at the first stage, the films were initially slowly heated to a temperature of about 200 °C (slightly below the melting point of tin 322 °C (*Metals and Alloys - Melting Temperatures*, no date)) and kept at this temperature for 2 hours. Then, at the second stage, the films were slowly heated to a temperature of 300 °C, 375 °C, or 450 °C, followed by isothermal annealing for 1 hour. During deposition, the target current was ~ 100-150 mA, the target voltage was ~ 250 V. The target-substrate distance was 4 cm.

The described method of synthesizing tin dioxide films made it possible to achieve more precise control of the stoichiometric oxygen content in the films. This led to obtaining films with a variable electrical conductivity, since oxygen vacancies are electron donors in them (Yurakov *et al.*, 2007).

The obtained samples are characterized by different values of electrical conductivity and different contents of nickel. The main factors affecting the crystal structure of the films are the oxygen content in the argon-oxygen plasma during reactive magnetron sputtering, the temperature of annealing in air, and the size of the ferromagnetic insert in the tin target.

In Figure 32 is shown the X-ray diffraction patterns of films obtained by sputtering a tin target in an argon plasma with one and two nickel strips 2 mm wide after annealing at 200 °C for 2 hours in the first stage and 375 °C for 1 hour in the second stage. From the X-ray diffraction patterns, it can be concluded that a polycrystalline film with a rather weak crystallinity is formed.

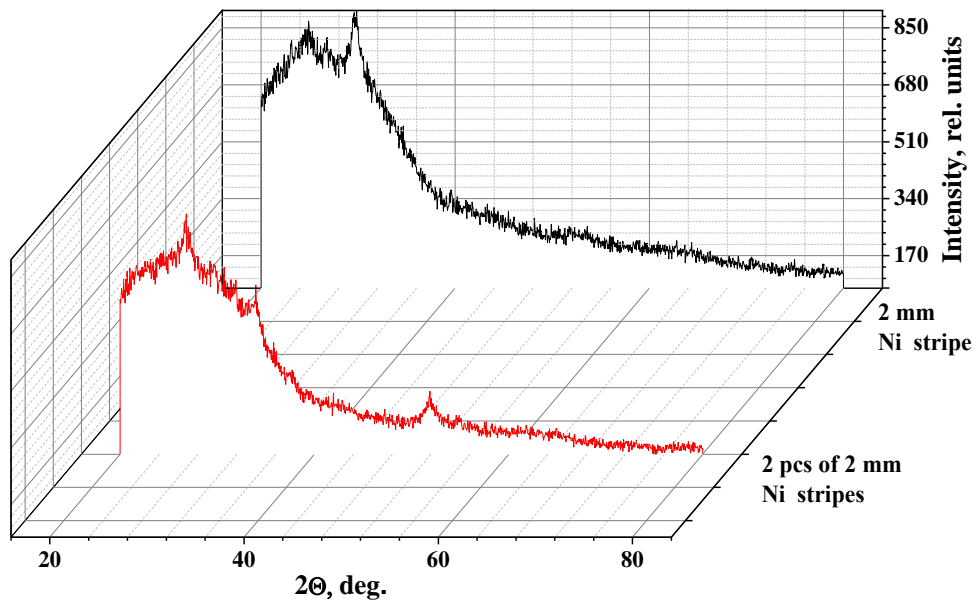


Figure 32. The X-ray diffraction patterns of films obtained by sputtering a tin target in an argon plasma with one and two nickel strips 2 mm wide.

Figure 33 shows the X-ray diffraction patterns of films obtained by sputtering a tin target in an argon plasma with two nickel strips 2 mm wide each after annealing at a temperature of 200 °C for 2 hours in the first stage and 375 °C for 1 hour in the second stage. These X-ray

diffraction patterns show the effect of the oxygen content in the argon-oxygen plasma on the structural properties of the films. It can be seen that a decrease in the intensity and an increase in the half-width of the peaks are observed with an increase in the oxygen content. It indicates a deterioration in the crystallinity of the film. Amorphous films are formed in the process of reactive magnetron sputtering with an oxygen content of 4 and 8 vol. % in argon-oxygen plasma.

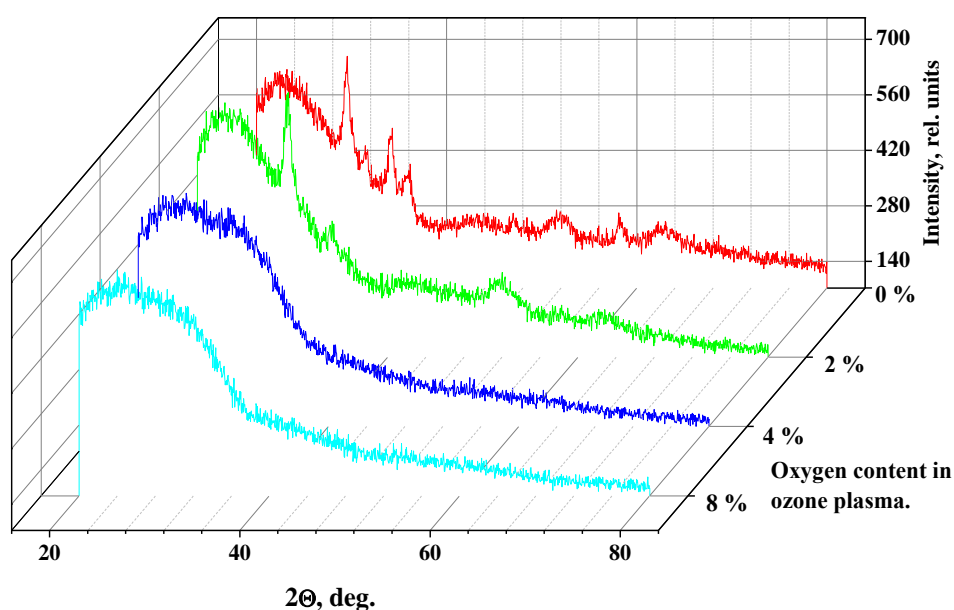


Figure 33. The X-ray diffraction patterns of films obtained by sputtering a tin target in an argon plasma with two nickel strips 2 mm wide each for different oxygen content.

### 3.4. Experimental setup

Experimental setup and its schematic diagram of humidity control system are shown in Figure 34 and Figure 35, respectively. The sample was placed in a gas cell of AFM for measurements. The RH of the air was changing in the gas cell through the humidity control system. Dry air is supplied to the setup, which is dividing into two parts using tube system. The airflow is controlled by a valve. One part of the air passes through the bubbler, where it is saturated with moisture. Then both parts of the flow are mixed again and enter the gas cell. A humidity sensor is installed at the entrance of the gas cell. The humidity sensor is connected to the Arduino Uno motherboard, which displays the sensor readings on the

screen. The sample is measured using an AFM, where a gas cell is installed. Measurement mode is PeakForce Kelvin Probe Force Microscopy.

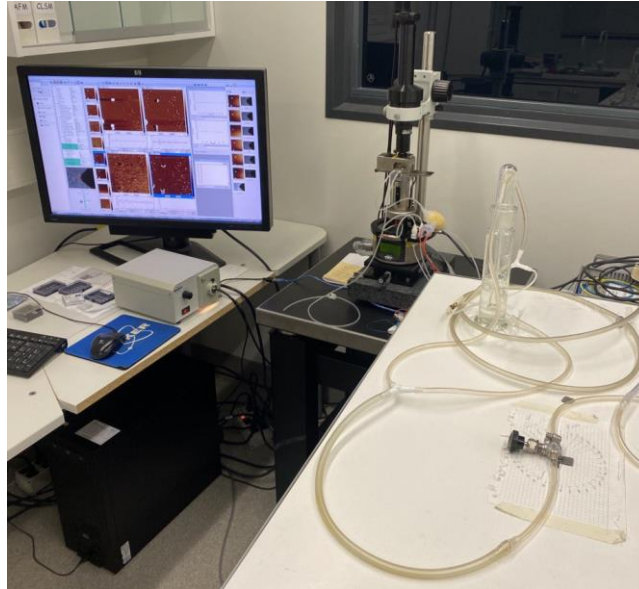


Figure 34. Experimental setup.

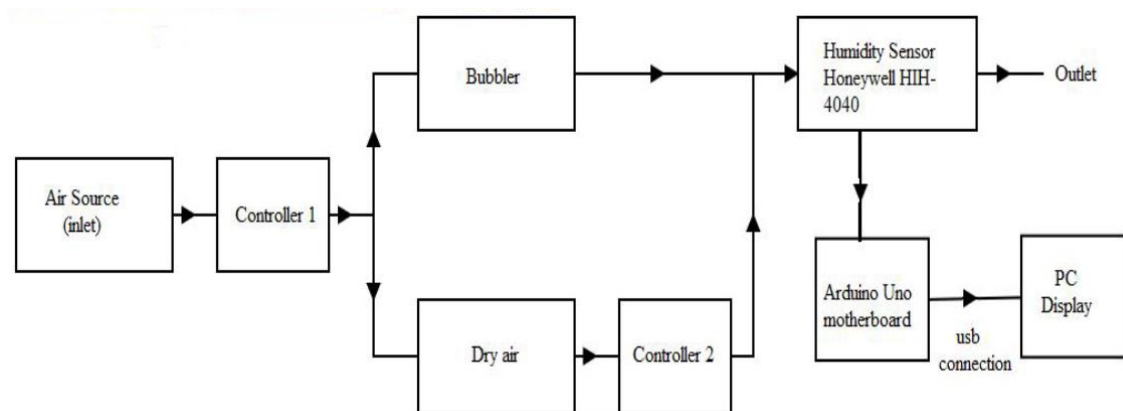


Figure 35. Schematic diagram of humidity control system (Rasheed, 2017).

Three samples were investigated. Three cycles of measurement were performed for each sample. One cycle includes increasing the RH from 10% to 80% and decreasing it back to 10%. Before each measurement, the humidity in the chamber was set for 20 minutes. It was done in order to stabilize the RH reading. RH was decreasing by 5% from the set value during the experiment. However, RH was decreasing by 10% from the highest set value of 80% RH. Scanning time was 16 minutes. The following parameters were used: scan size was  $3 \times 3 \mu\text{m}$ , resolution was 128 samples/line, and scan rate was 0.25 Hz. PFQNE-A1 probe was used, and scanning direction was from down to top.

## 4. Measurement results

Three samples with different oxygen content and with one or two nickel strips were selected for measurements. Sample #1 was obtained using two strips of nickel 2 mm wide (4 mm in total) and 0 vol. % oxygen in argon plasma. This sample has the least resistance. Sample #2 was obtained using two strips of nickel 2 mm wide (4 mm in total) and 4 vol. % oxygen in argon plasma. This sample has the highest resistance. Sample #3 was obtained using one strip of nickel 2 mm wide and 0 vol. % oxygen in argon plasma. Its resistance has the median value.

### 4.1. Sample #1 with 4 mm Ni and 0% O<sub>2</sub>

The height topography and potential of the sample during the first cycle are shown in Figure 36. The RH were cycled through the values 20% - 40% - 80% - 40% - 10%. Comparison of the Gaussian peak functions of potential for the first cycle of the measurement is shown in Figure 37 (a). The width of the peak decreases with a change in RH from 20% to 40%. The further change in humidity leads to the change of the peak's width upward. The central value of the potential decreases, i.e. shifts to the left, with a decrease in humidity from 80% to 40%, in other cases the central value increases. The amplitude value, i.e. the height of the histogram peak, also has no clear dependence, alternately increasing and decreasing. However, it should be noted that at 40% of RH, the potential value coincides in cycles with increasing and decreasing humidity.

The depth histogram and its amplitude version of the Gaussian peak function of the potential for 20% RH are presented in Figure 38. The depth histogram is the distribution of particles with certain electrical potential value. Thus, this histogram shows what percentage of particles has a certain potential value.

In Figure 39 is shown photographs of the surface for 0% RH and 95% RH using an optical microscope (OM). The number of black dots on the surface increases and their size also increases with the increase of RH. It may indicate the surface expansion. The topography map (Figure 40) shows that the surface undergoes changes as the humidity changes. After the RH rises to 80%, the scan result is blurry and remains so until the third cycle. This may be due to the sample's saturation with moisture and undergoes changes. Thus, the sample can increase in volume or become softer, which affects crucially the scanning process.

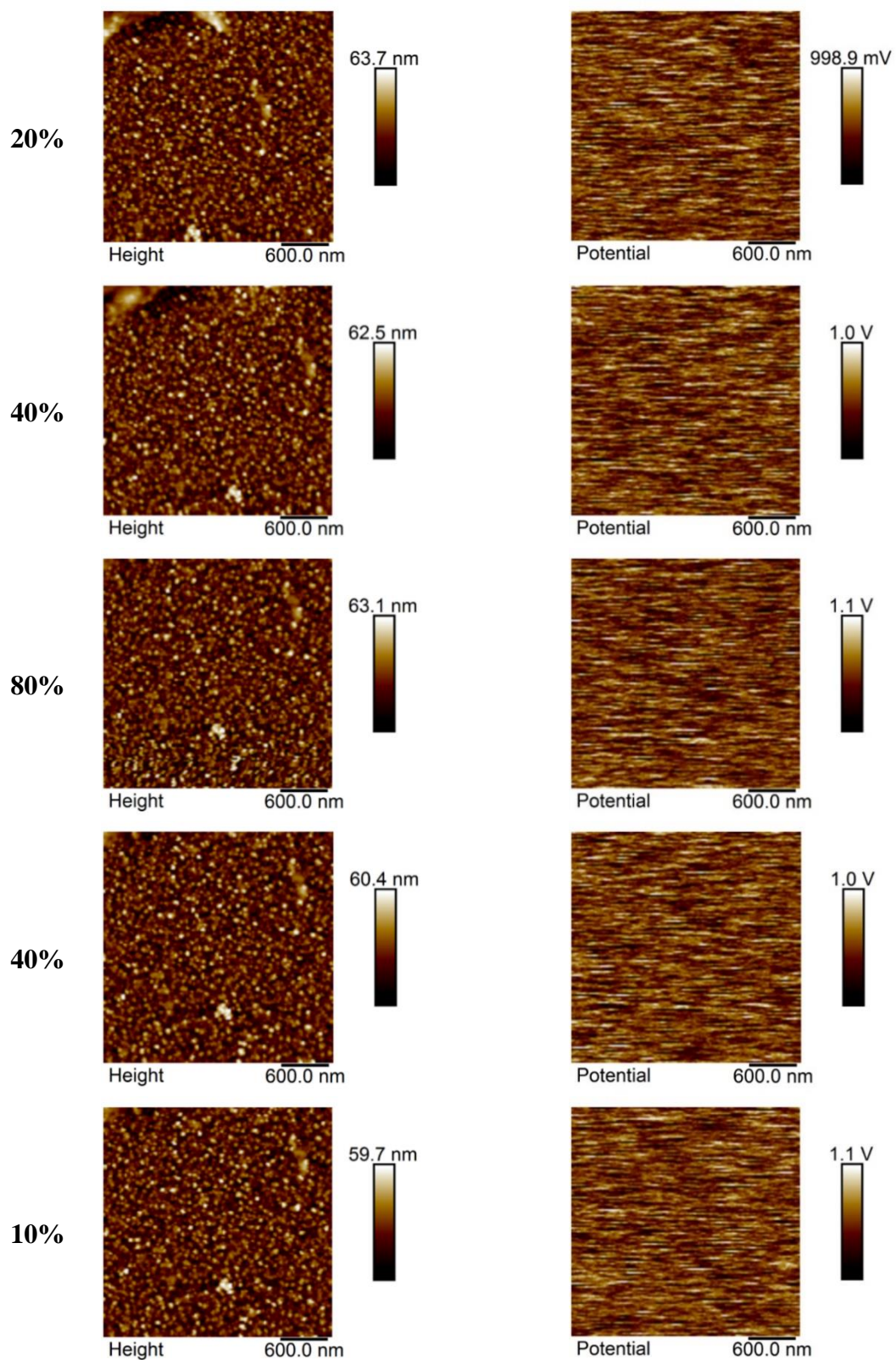


Figure 36. AFM images of topography (left) and electric potential map (right) of the sample #1 during the first measurement cycle 20%-40%-80%-40%-10%.

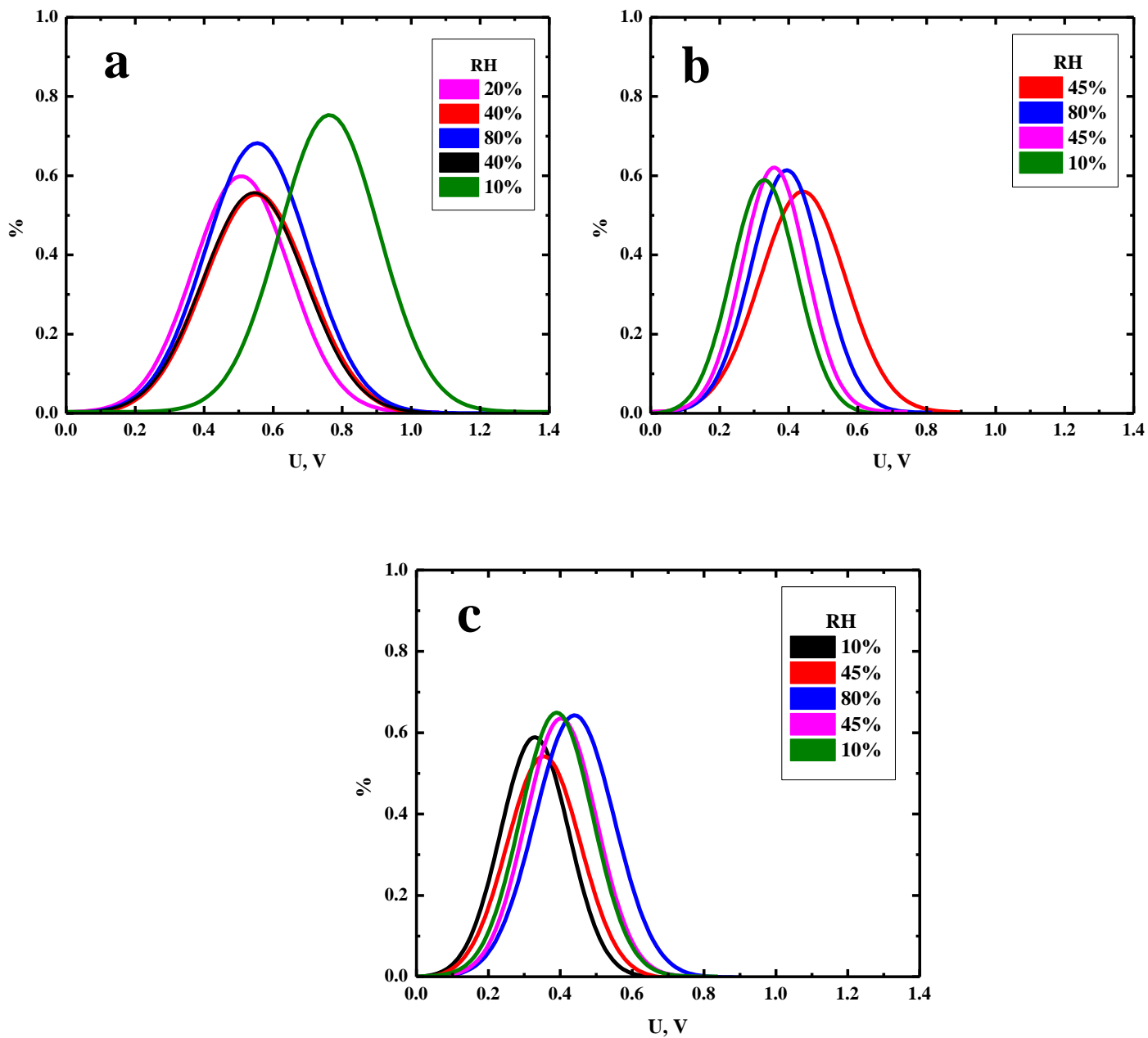


Figure 37. Gaussian peak functions of electric potential during the RH changing of the sample #1. (a) the first cycle; (b) the second cycle; (c) the third cycle.

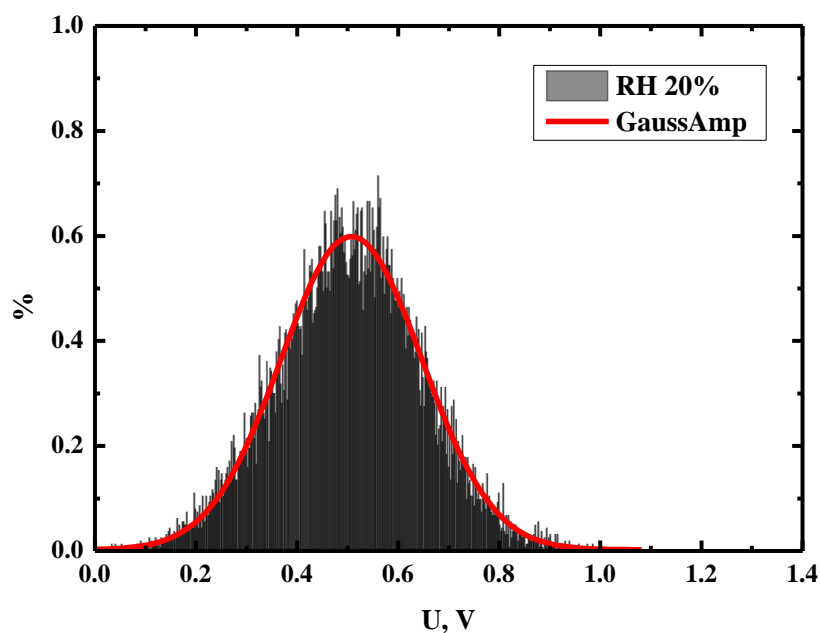


Figure 38. Depth histogram and its amplitude version of the Gaussian peak function of the potential for RH of 20%.

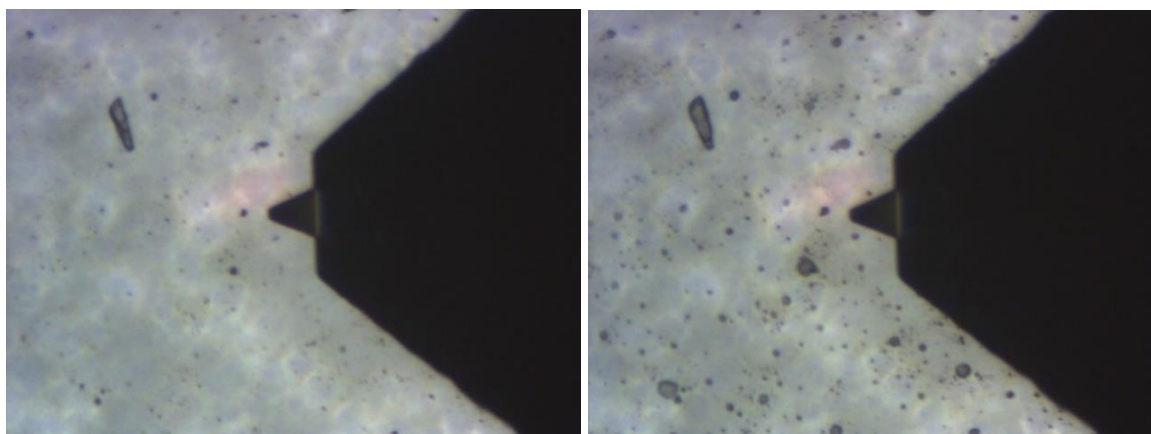


Figure 39. Photographs of the sample #1 surface for 0% RH (left) and 95% RH (right) using an OM. Optical resolution is 500x375  $\mu\text{m}$ .

The next two cycles were done in a different area, and thus cannot be compared directly with the first cycle. The RH was 45% - 80% - 45% - 10% - 45% - 80% - 45% - 10%. The topography and potential map during the experiment are shown in Figure 40 and Figure 41. The Gaussian fits of potential histogram for the second and the third cycles is shown in Figure 37 (b) and (c) respectively.

The potential value was going down during the entire second cycle with any change in humidity. That can be seen in the Figure 37 (b). The peak amplitude is increasing during cycle 45% - 80% - 45% and decreasing when RH goes from 45% to 10%. At the same time, the peak width has opposite correlation; it becomes narrower in a cycle 45% - 80% - 45% and it broadens at 10% humidity. The dependence of the film potential on the RH during the third cycle is shown in Figure 37 (c). The potential shifts respective to RH changes. The potential grows with humidity increasing and drops during RH declining.

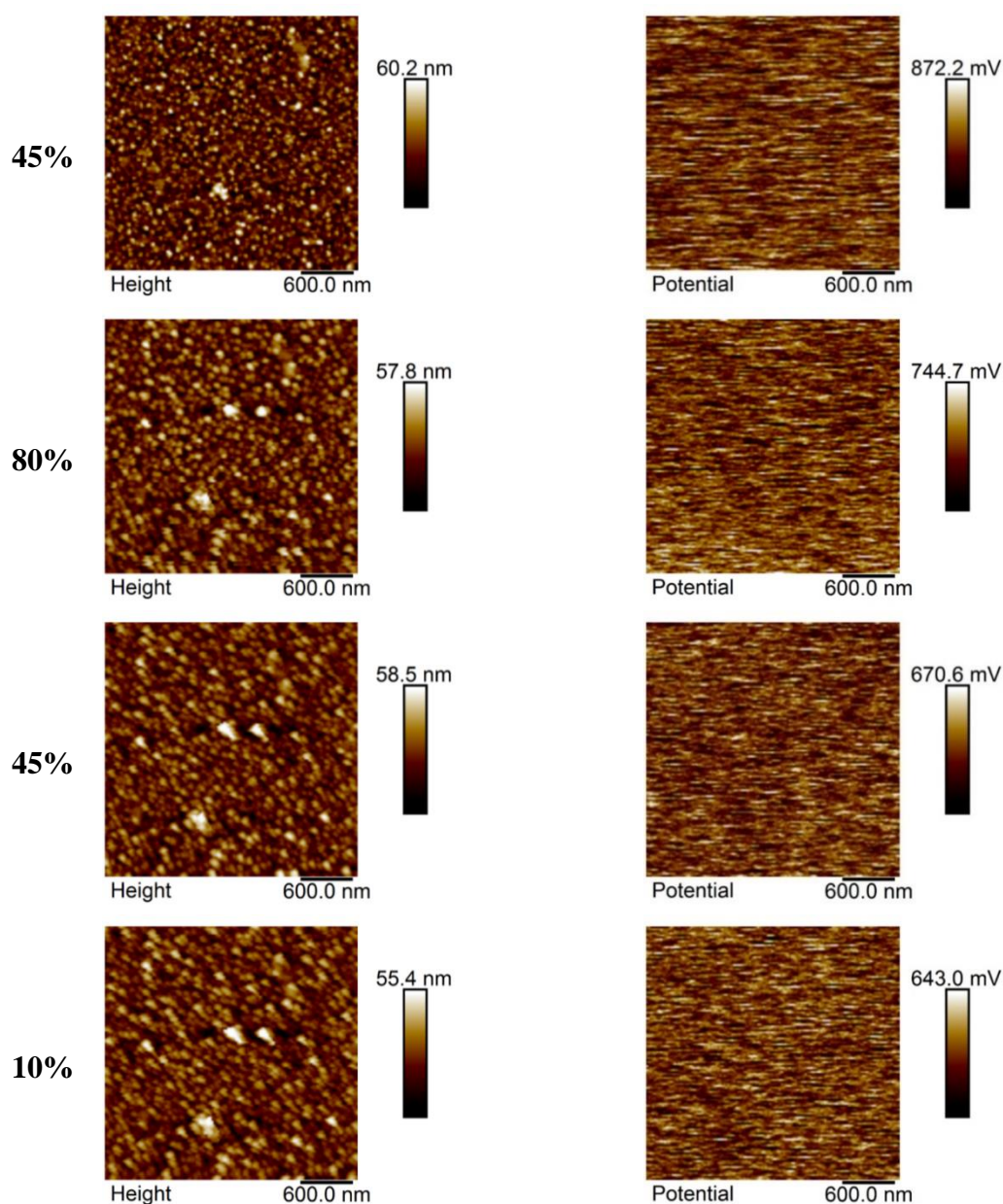


Figure 40. Topography (left) and potential (right) maps of the sample #1 during the second measurement cycle 45%-80%-45%-10%.

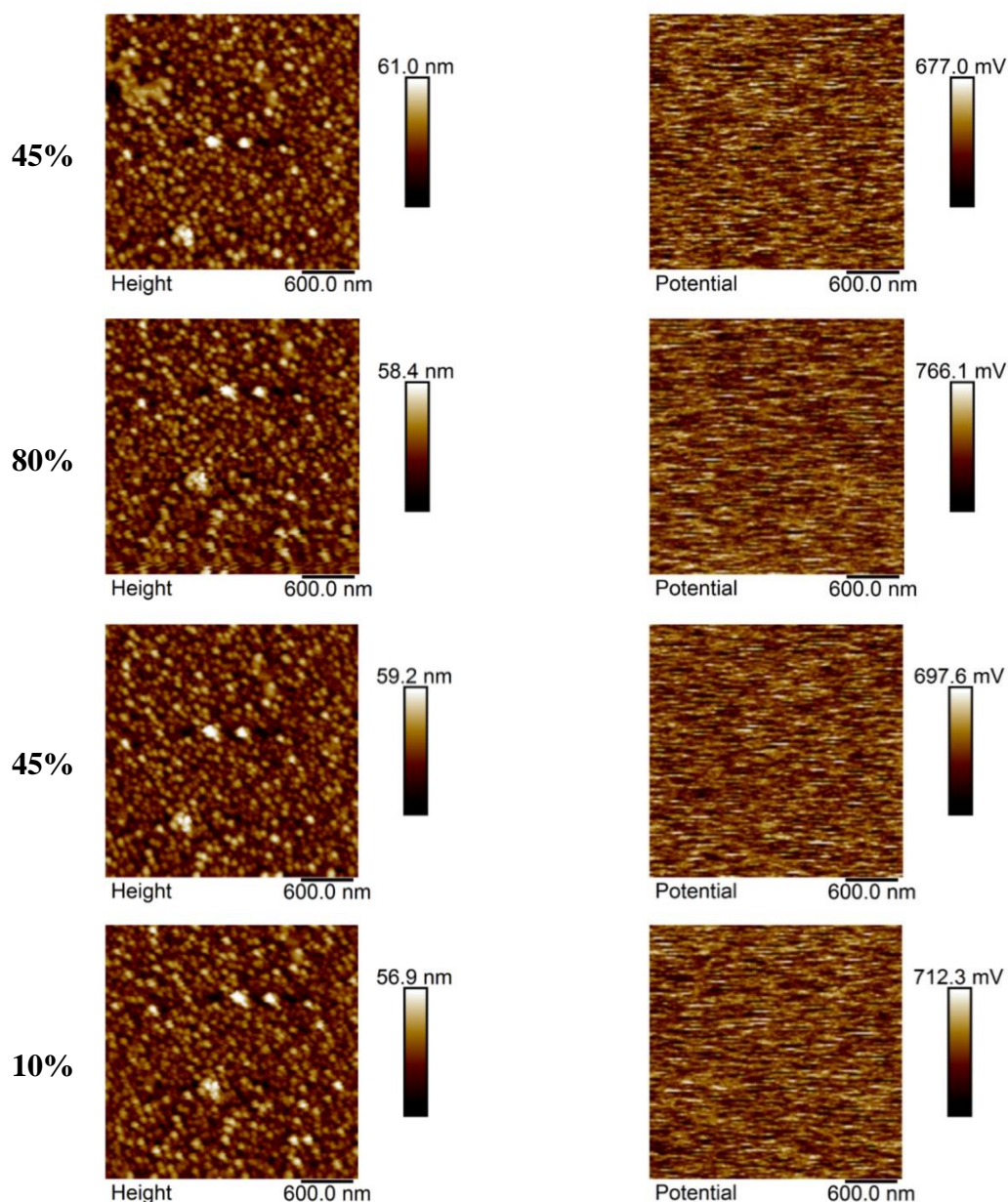


Figure 41. Topography (left) and potential (right) maps of the sample #1 during the third measurement cycle 45%-80%-45%-10%.

Since the probe itself also contributes to the potential change, it is necessary to subtract this influence from the obtained results. Better understanding of the nature of this phenomenon required additional measurements of simple aluminum and copper foil. An additional bias of 1 V was applied for aluminum foil to offset the entire potential level to the zero. The changing of the Gaussian peaks during humidity changing for the aluminum and copper foils is shown in Figure 42. Figure 43 compares the Gaussian peaks for the first measurement cycle of the sample #1 and for copper foil.

An amplitude version of Gaussian peak function curve is described in Figure 44, where  $A$  is amplitude of the Gaussian peak,  $w$  is its width,  $x_c$  is the center value of the peak and  $y_0$  is the offset.

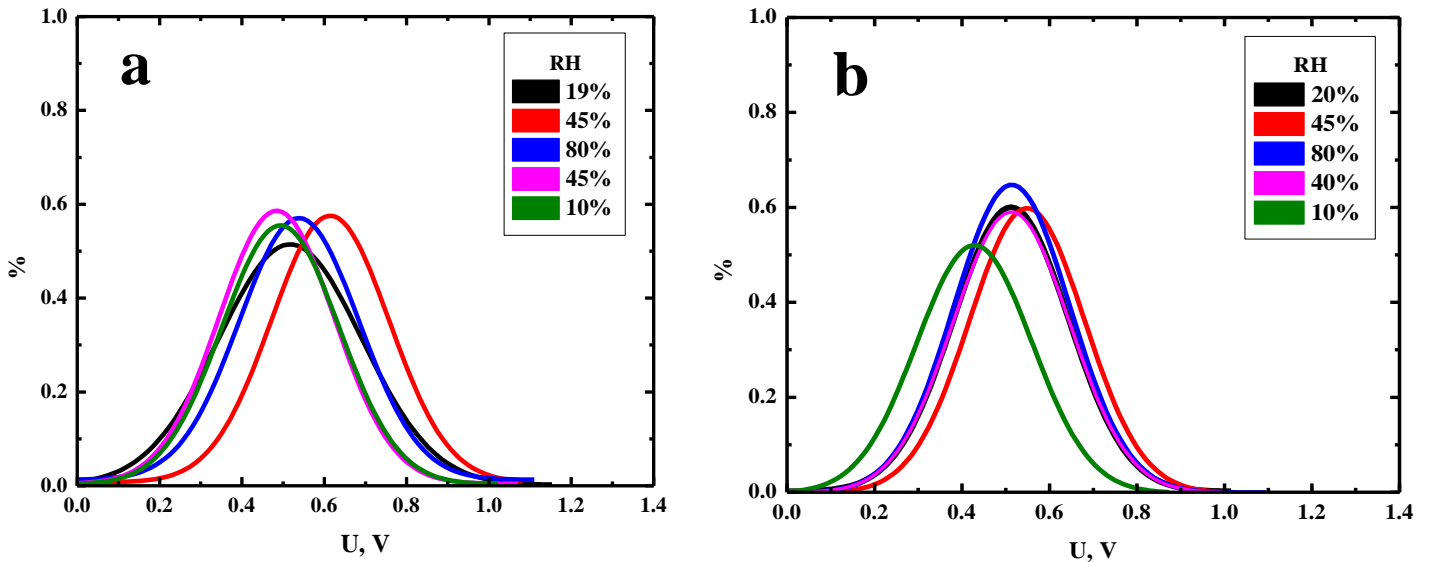


Figure 42 – Gaussian peak functions of electric potential during the RH changing (a) for the aluminum foil; (b) for the copper foil.

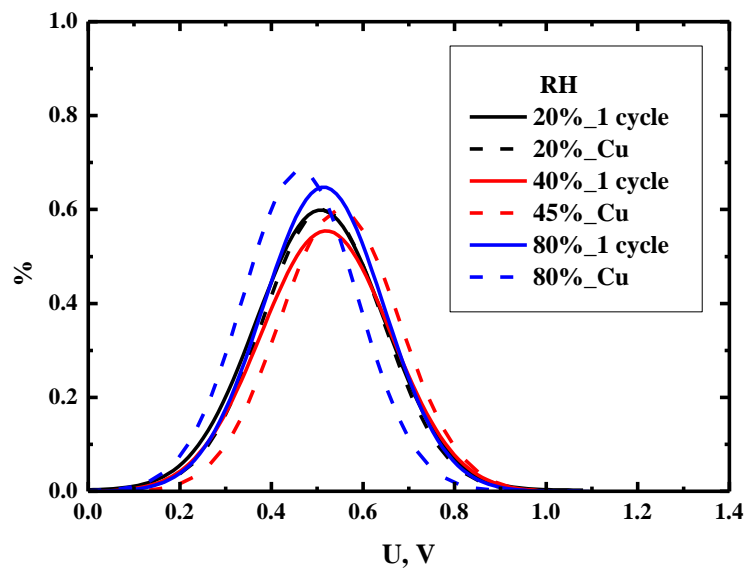


Figure 43. Comparison of the Gaussian peaks for the first measurement cycle of the sample #1 and for copper foil.

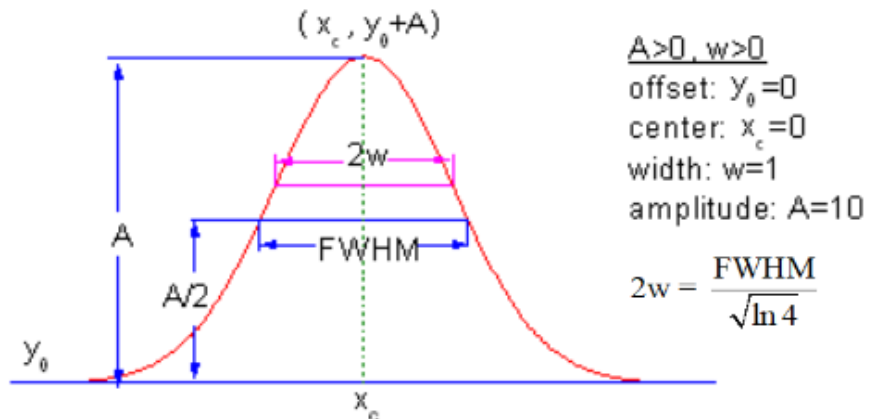


Figure 44. An amplitude version of Gaussian peak function curve (*Help Online - Origin Help - GaussAmp*, no date).

Table 1 shows the main parameters of the Gaussian peaks for all measurements. This allows the analysis of the potential distribution. Table 2 shows the change in potential during measurements. It represents the differences in the parameters' values between the previous measurement and the next one, i.e.  $A = A_i - A_{i+1}$ , where  $i$  is the serial number of measurement. Thus, the negative value in the table means that the parameter value has increased. Also this data in these tables does not indicate any correlation between RH and potential value.

Table 1. The main parameters of the Gaussian peaks for all measurements of the sample #1.

RH	Parameters	1 cycle	2 cycle	3 cycle	Cu	Al
20%	$x_c$	0.507	-	0.329	0.512	0.517
	$A$	0.597	-	0.591	0.599	0.513
	$FWHM$	0.329	-	0.223	0.309	0.410
45%	$x_c$	0.549	0.441	0.354	0.549	0.614
	$A$	0.556	0.558	0.546	0.600	0.568
	$FWHM$	0.352	0.292	0.241	0.309	0.337
80%	$x_c$	0.553	0.395	0.440	0.514	0.539
	$A$	0.682	0.612	0.645	0.648	0.558
	$FWHM$	0.352	0.242	0.260	0.312	0.342
45%	$x_c$	0.545	0.358	0.403	0.513	0.484
	$A$	0.556	0.617	0.635	0.591	0.582
	$FWHM$	0.349	0.218	0.233	0.313	0.331
10%	$x_c$	0.763	0.329	0.390	0.428	0.494
	$A$	0.750	0.591	0.649	0.522	0.552
	$FWHM$	0.341	0.224	0.237	0.3104	0.335

Table 2. The differences in the parameters' values between the previous and the next measurement for the sample #1.

Parameters	RH	1 cycle	2 cycle	3 cycle	Cu	Al
$x_c$	20% - 45%	-0.041	-	-0.025	-0.036	-0.097
	45% - 80%	-0.005	0.047	-0.085	0.035	0.076
	80% - 45%	0.009	0.037	0.037	0.001	0.054
	45% - 10%	-0.218	0.029	0.013	0.084	-0.009
A	20% - 45%	0.041	-	0.045	-0.001	-0.056
	45% - 80%	-0.126	-0.054	-0.098	-0.049	0.010
	80% - 45%	0.126	-0.006	0.009	0.058	-0.024
	45% - 10%	-0.193	0.026	-0.014	0.069	0.030
FWHM	20% - 45%	-0.023	-	-0.017	-0.0003	0.073
	45% - 80%	0.0004	0.049	-0.020	-0.002	-0.005
	80% - 45%	0.003	0.025	0.027	-0.002	0.012
	45% - 10%	0.007	-0.006	-0.004	0.003	-0.004

Change of the position of the maximum of the Gaussian curve during the change in RH for three measurement cycles is shown in Figure 45. The presented graphs take into account the influence of the probe on the potential change. It was done by subtraction the average value of copper and aluminum foils potential from the obtained values, i.e.  $X_c(new) = X_c - X_c(foil)$ , where  $X_c(foil) = [X_c(Cu) + X_c(Al)]/2$ . It can be seen from the Figure 45 that the 1<sup>st</sup> and the 3<sup>rd</sup> cycles have similar curves. Between 20% and 45% RH voltage goes down. After it increases until 80% RH and decreases until 45% RH. From 45% to 10% RH goes up again. The 2<sup>nd</sup> cycle's curve also has similar dependence; however, the amplitude fluctuation of the potential is smaller.

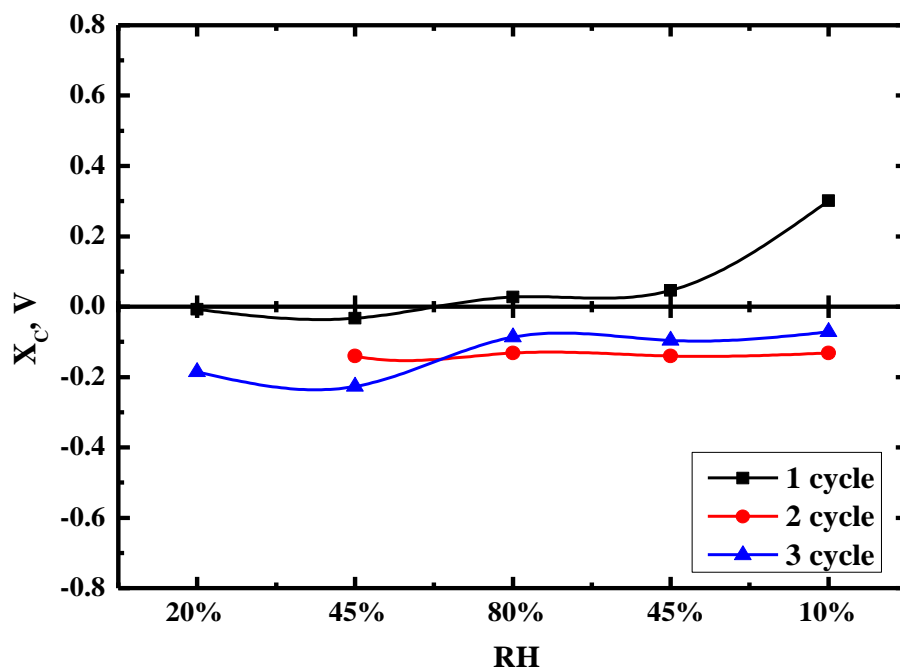


Figure 45 – Change in the position of the maximum of the Gaussian curve during the change in RH for three measurement cycles of the sample #1.

#### 4.2. Sample #2 with 4 mm Ni and 4% O<sub>2</sub>

4 mm nickel with 4% oxygen film was chosen as the second sample. The height topography and the potential value of the sample during three cycles are shown in Figure 46, Figure 47 and Figure 48. The RH were 15% - 45% - 80% - 45% - 10% - 45% - 80% - 45% - 10% - 45% - 80% - 45% - 10%. The comparison of the Gaussian peak functions of potential for three cycles of the measurement is presented in Figure 49. Figure 50 shows photographs of the surface for 10% RH and 80% RH using an OM. It can be seen that there is no difference between them, so the surface of the sample does not expand from moisture.

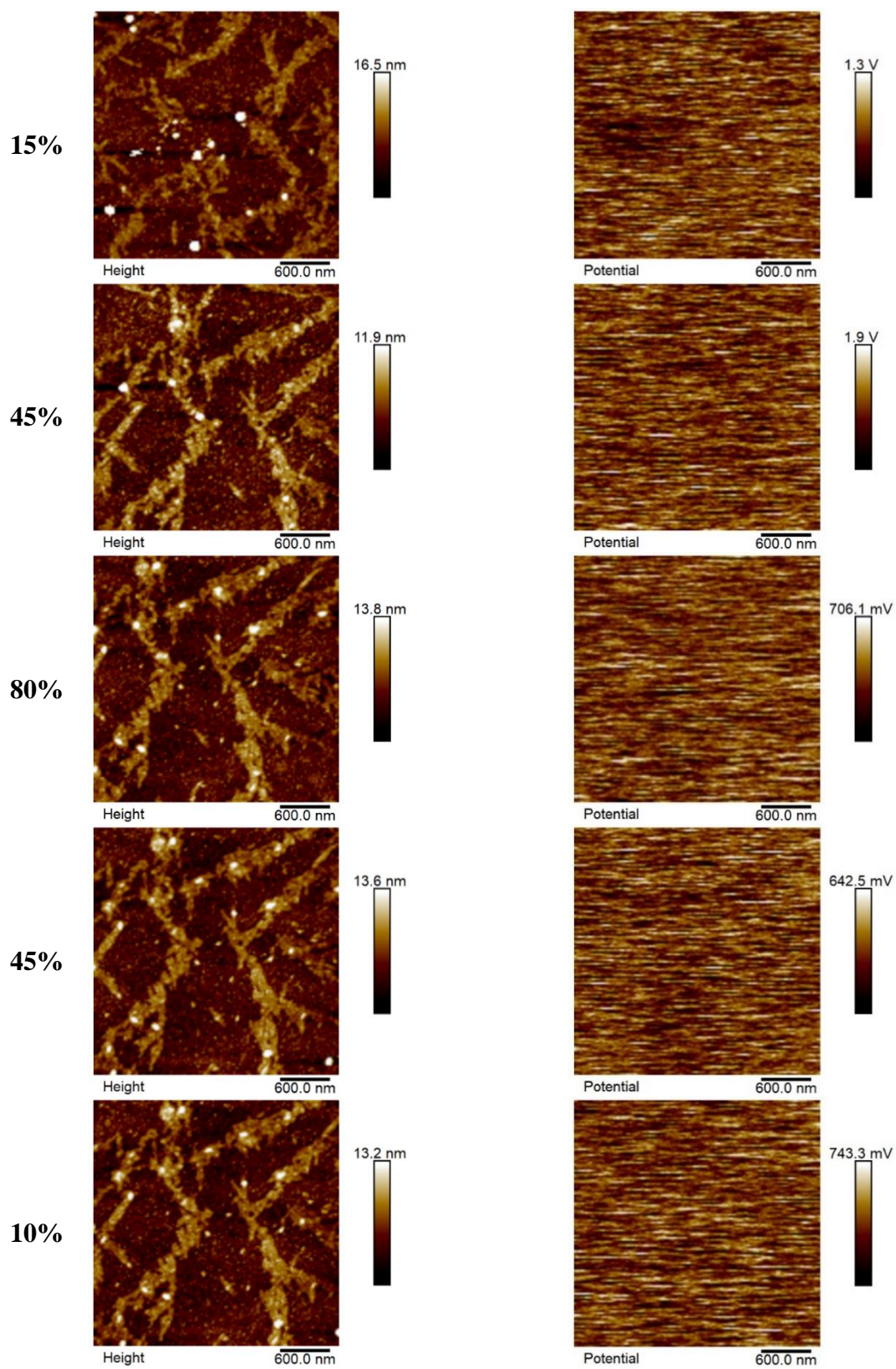


Figure 46. AFM images of topography (left) and potential map (right) of the sample #2 during the first measurement cycle 15%-45%-80%-45%-10%.

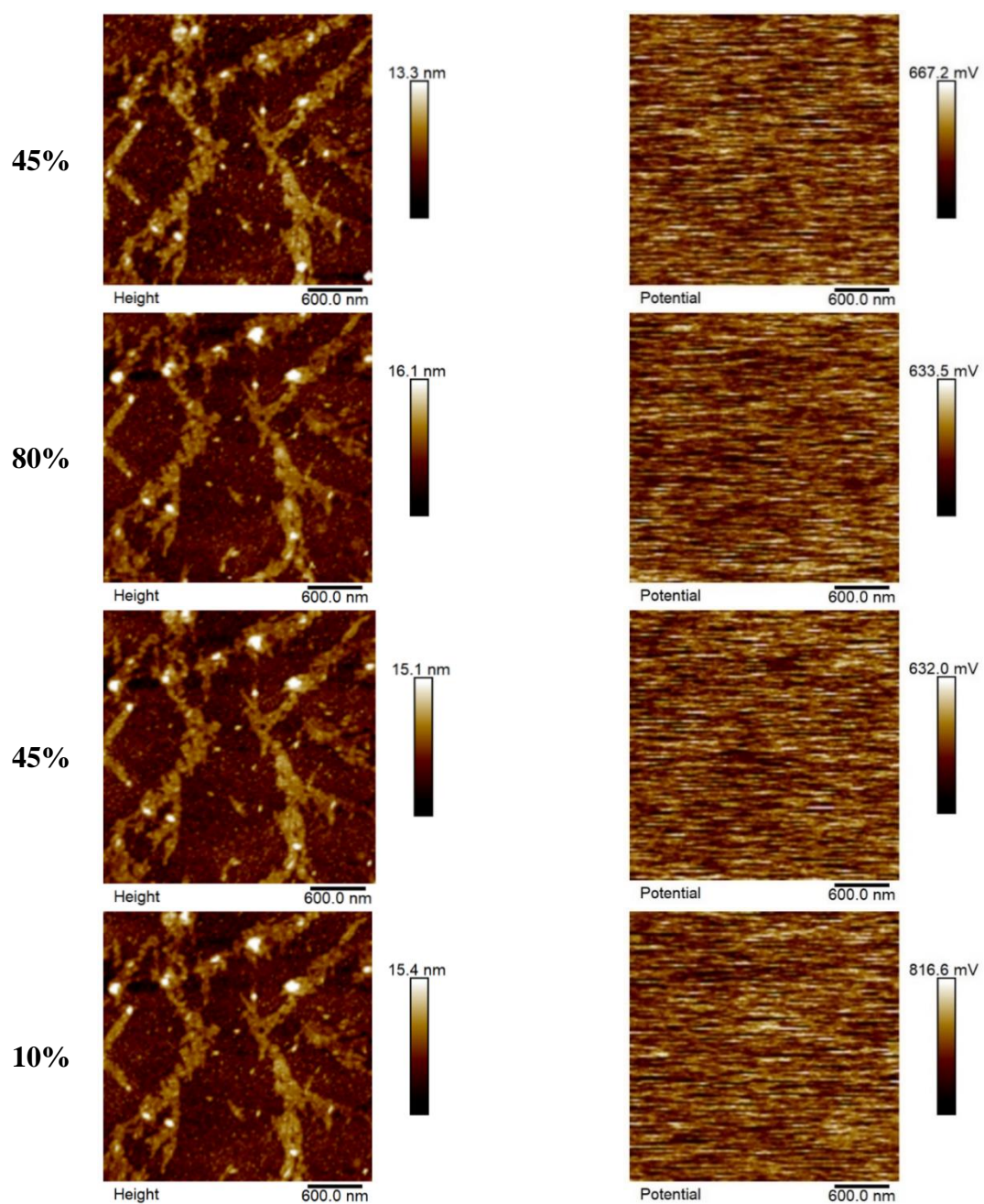


Figure 47. AFM images of topography (left) and potential map (right) of the sample #2 during the second measurement cycle 45%-80%-45%-10%.

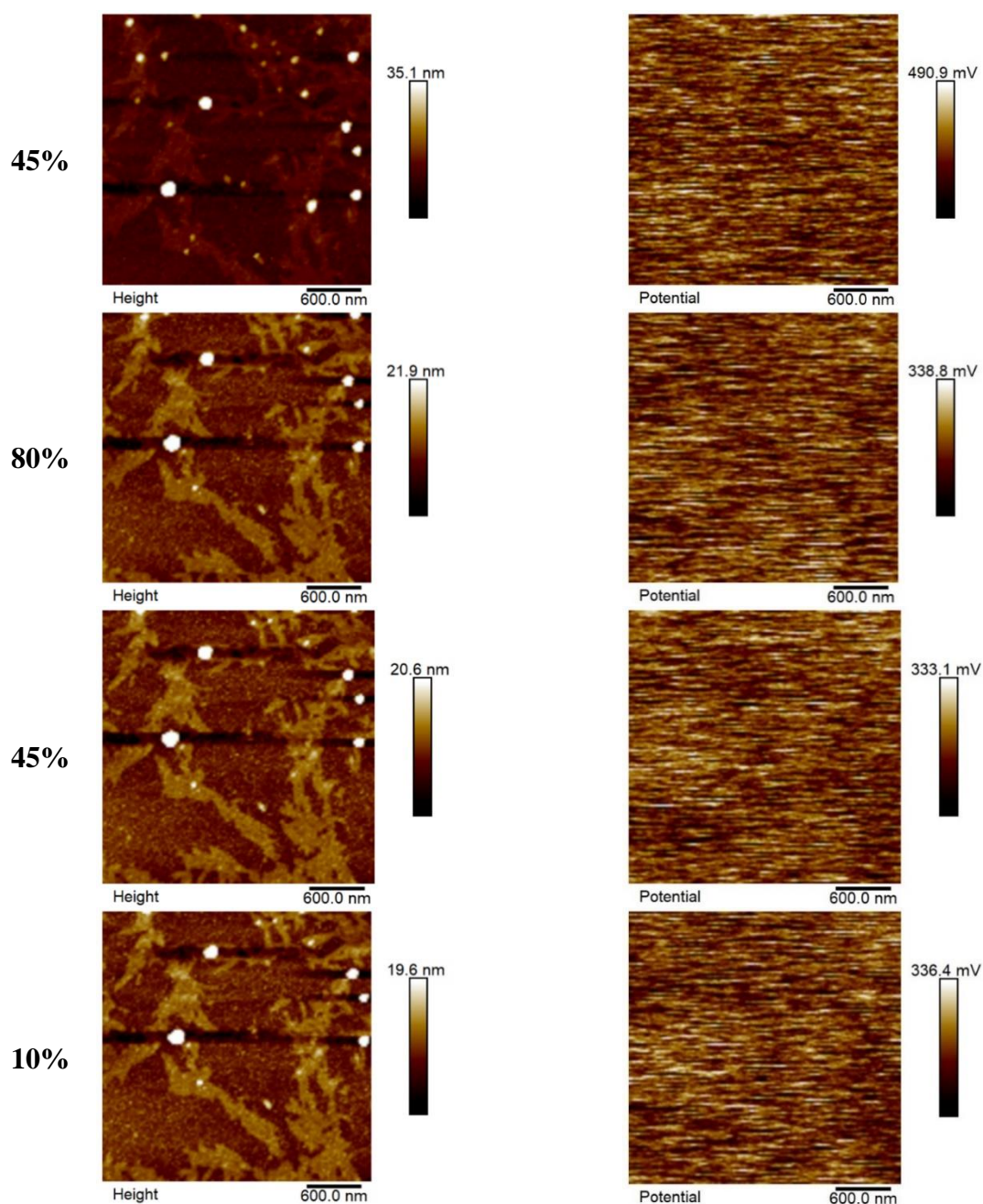


Figure 48. AFM images of topography (left) and potential map (right) of the sample #2 during the third measurement cycle 45%-80%-45%-10%.

Gaussian peaks for the 1<sup>st</sup> cycle are shown in Figure 49 (a). It is visible that potential value is increasing with increasing the RH from 15% to 45%. During the 45% - 80% - 45% changes potential is gone down, and after it rises again with 45%-10% RH change. The highest Gaussian curve amplitude is achieved with 80% RH. Largest spread of potential values corresponds to the first 45% RH.

Gaussian peaks for the 2<sup>nd</sup> cycle are shown in Figure 49 (b). It is noticeable that the potential almost does not change when the RH changes 45%-80%-45%. Peaks of 10% RH have the highest potential central values and they are broader compared to the rest of the peaks.

The 3<sup>rd</sup> cycle of measurement is presented in Figure 49 (c). All curves shift left and become narrower during the cycle except last change from 45% to 10% RH. However, after 45%-10% RH change the amplitude of the peak reached the maximum value.

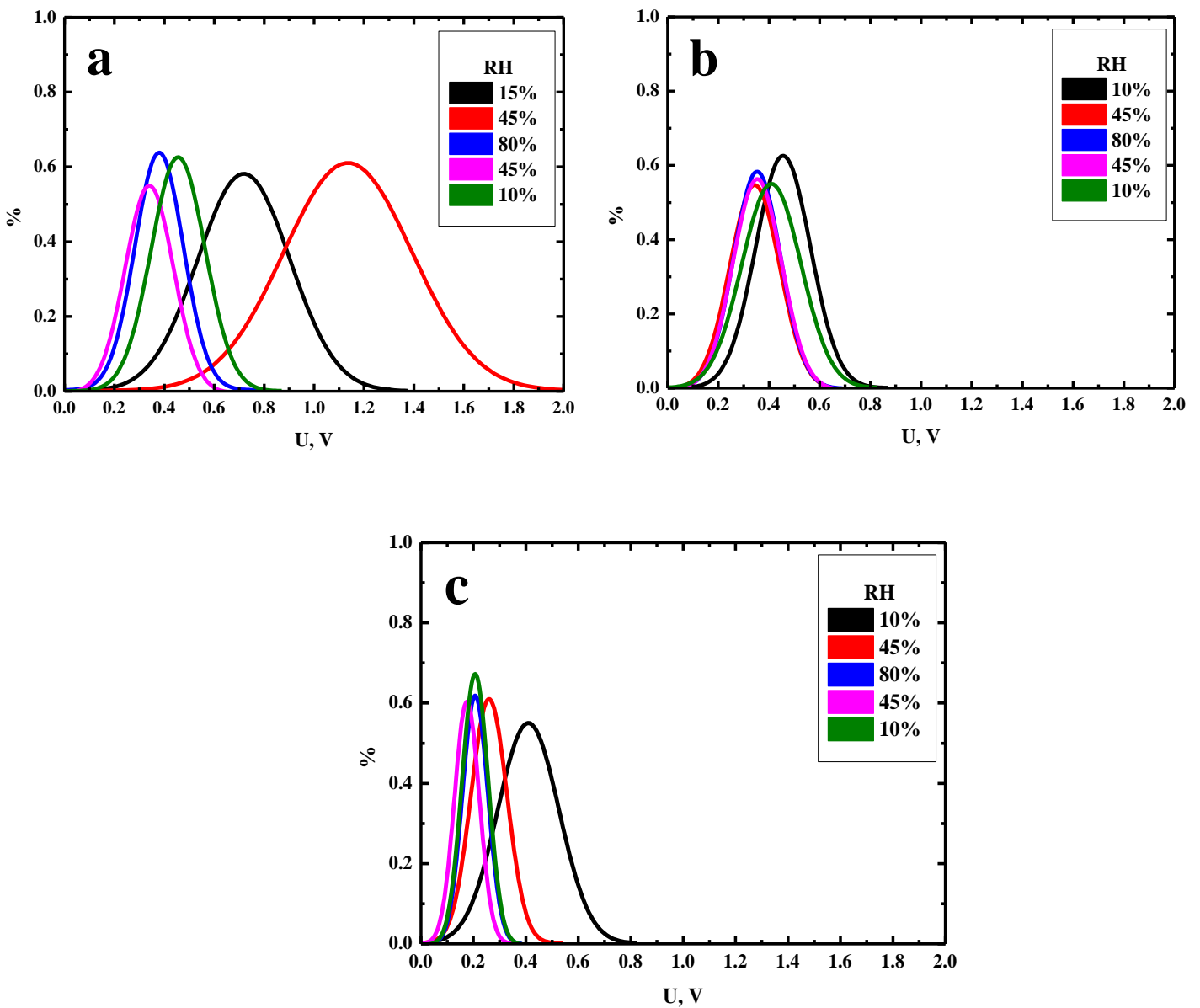


Figure 49. Gaussian peak functions of electric potential during the RH changing of the sample #2. (a) the first cycle; (b) the second cycle; (c) the third cycle.

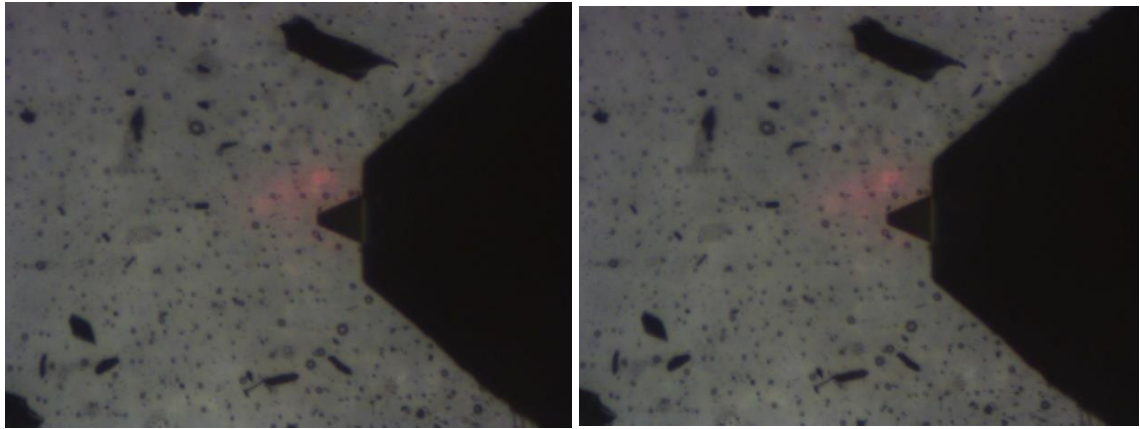


Figure 50. Photographs of the sample #2 surface for 10% RH (left) and 80% RH (right) using an OM. Optical resolution is 500x375  $\mu\text{m}$ .

Table 3 shows the main parameters of the Gaussian peaks for all measurements for sample #2. This allows the analysis of the potential distribution. Table 4 shows the change in electric potential during measurements. It represents the differences in the parameters' values between the previous measurement and the next one, i.e.  $A=A_i - A_{i+1}$ , where  $i$  is the serial number of measurement. Thus, the negative value in the table means that the parameter value has increased.

Table 3. The main parameters of the Gaussian peaks for all measurements of the sample #2.

RH	Parameters	1 cycle	2 cycle	3 cycle
10%	$x_c$	0.718	0.456	0.410
	$A$	0.582	0.626	0.550
	$FWHM$	0.433	0.255	0.275
45%	$x_c$	1.136	0.344	0.260
	$A$	0.609	0.551	0.609
	$FWHM$	0.608	0.230	0.162
80%	$x_c$	0.379	0.353	0.207
	$A$	0.635	0.585	0.619
	$FWHM$	0.228	0.218	0.114
45%	$x_c$	0.340	0.354	0.175
	$A$	0.555	0.568	0.603
	$FWHM$	0.227	0.226	0.111
10%	$x_c$	0.456	0.410	0.207
	$A$	0.626	0.550	0.675
	$FWHM$	0.255	0.275	0.117

Table 4. the differences in the parameters' values between the previous measurement and the next one for the sample #2.

Parameters	RH	1 cycle	2 cycle	3 cycle
$x_c$	10% - 45%	-0.417	0.112	0.150
	45% - 80%	0.756	-0.009	0.053
	80% - 45%	0.039	-0.001	0.032
	45% - 10%	-0.116	-0.056	-0.032
$A$	10% - 45%	-0.028	0.075	-0.059
	45% - 80%	-0.026	-0.034	-0.011
	80% - 45%	0.080	0.017	0.016
	45% - 10%	-0.071	0.018	-0.072
$FWHM$	10% - 45%	-0.173	0.025	0.113
	45% - 80%	0.379	0.012	0.048
	80% - 45%	0.001	-0.007	0.003
	45% - 10%	-0.028	-0.049	-0.006

Change in the position of the maximum of the Gaussian curve during the change in RH for three measurement cycles is represented in Figure 51. The presented graphs take into account the influence of the probe on the potential change. It was done by subtracting the average value of copper and aluminum foils potential from the obtained values.

In comparison to previous sample, potential has similar behavior during the 2<sup>nd</sup> and the 3<sup>rd</sup> cycles. However, the amplitude of potential changes for this sample is bigger. The potential changes during the 1<sup>st</sup> cycle do not show results analogous to others.

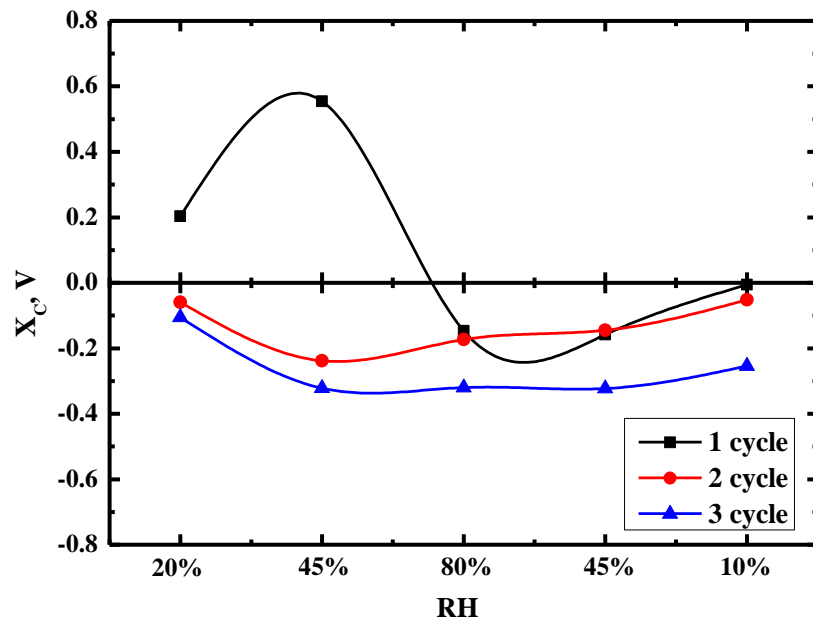


Figure 51. Change in the position of the maximum of the Gaussian curve during the change in RH for three measurement cycles of the sample #2.

#### 4.3. Sample #3 with 2 mm Ni and 0% O<sub>2</sub>

2 mm nickel with 0% oxygen film was chosen as the third sample. The height topography and the protentional map of the third sample during three cycles are shown in Figure 52, Figure 53 and Figure 54. It can be seen that the scanning area was shifted a bit during the experiment. At the same time, there is some high blobs on scans, which affect the final result.

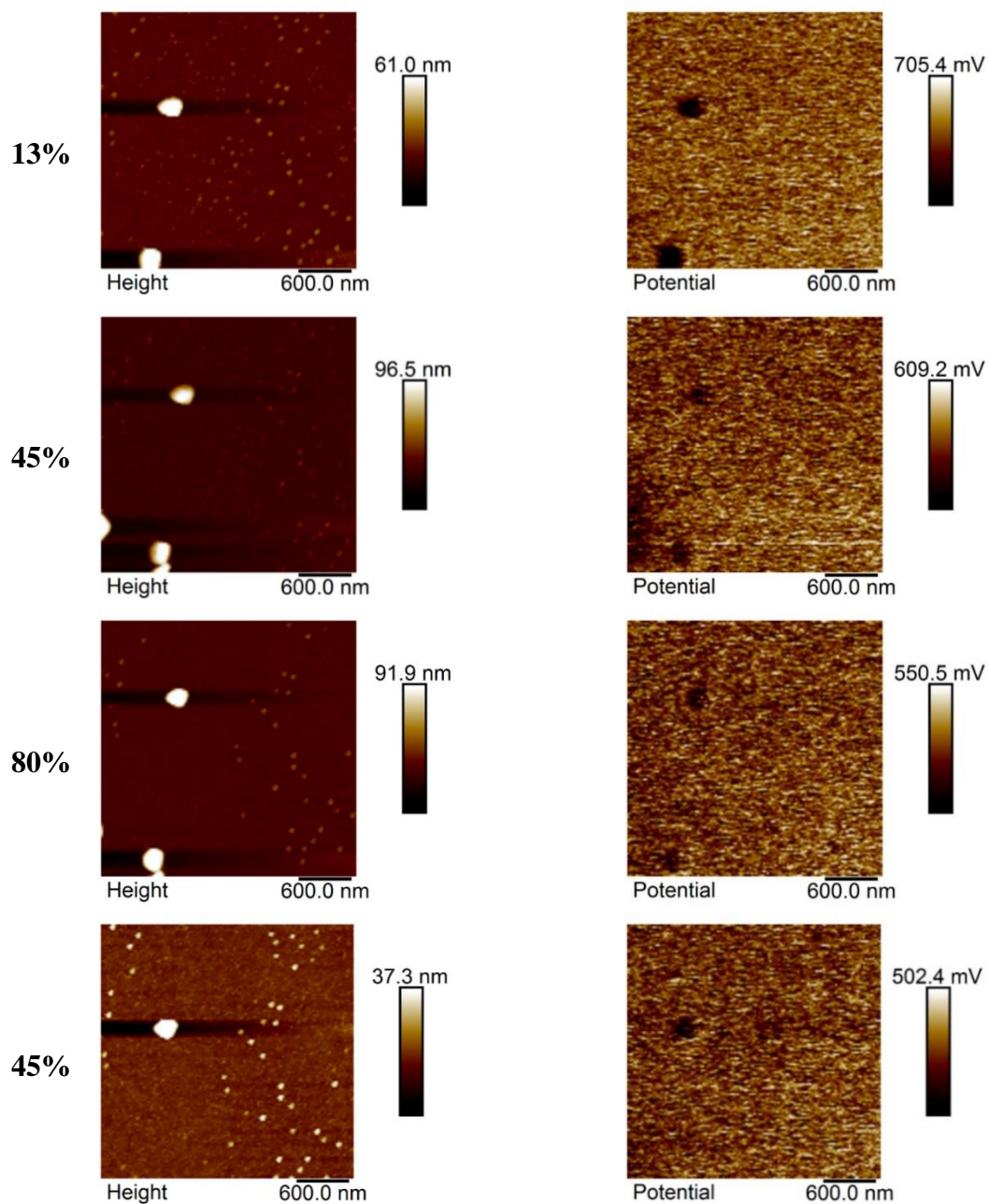


Figure 52. AFM images of topography (left) and potential map (right) of the sample #3 during the first measurement cycle 13%-45%-80%-45%.

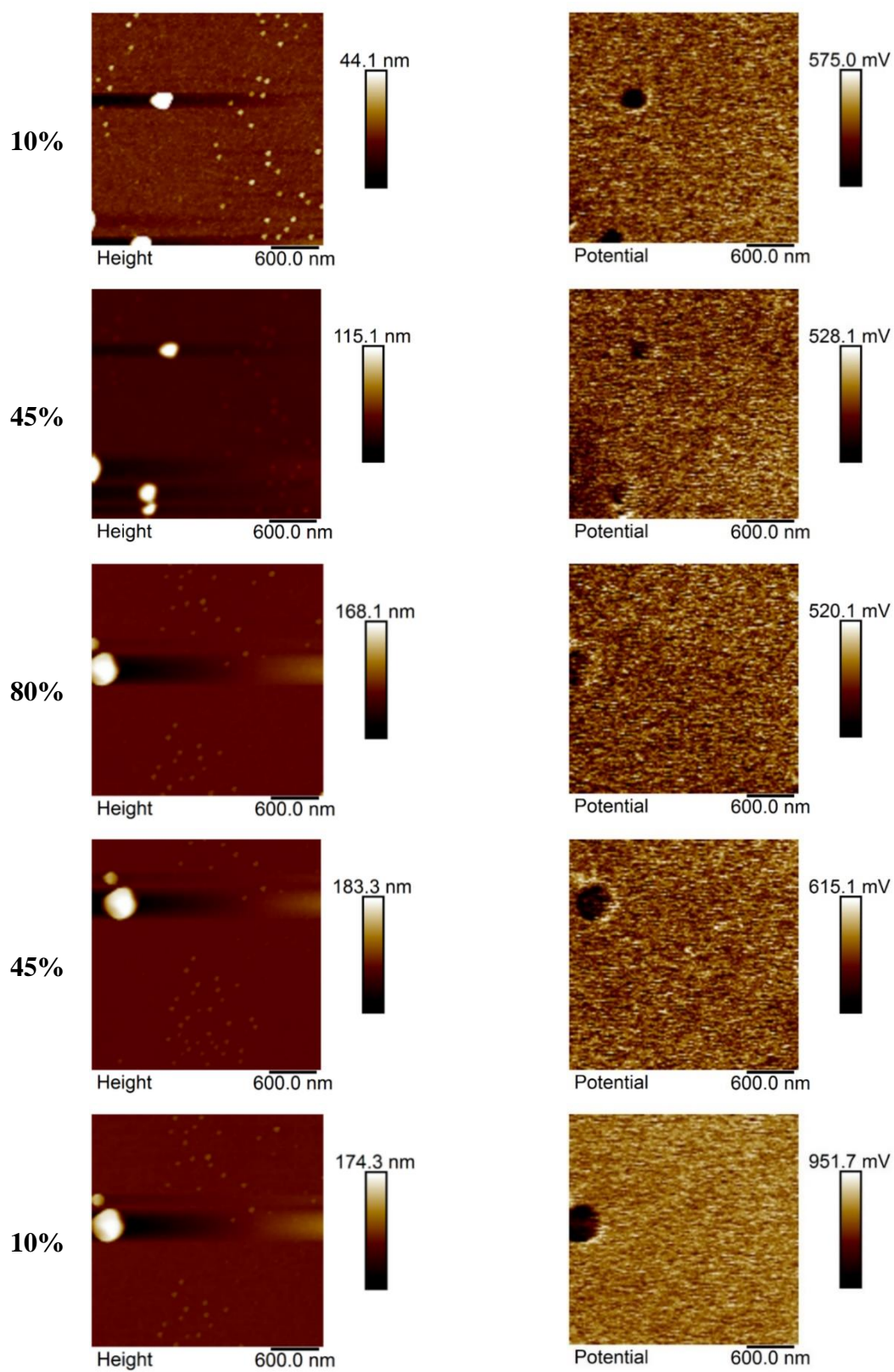


Figure 53. AFM images of topography (left) and potential map (right) of the sample #3 during the second measurement cycle 10%-45%-80%-45%-10%.

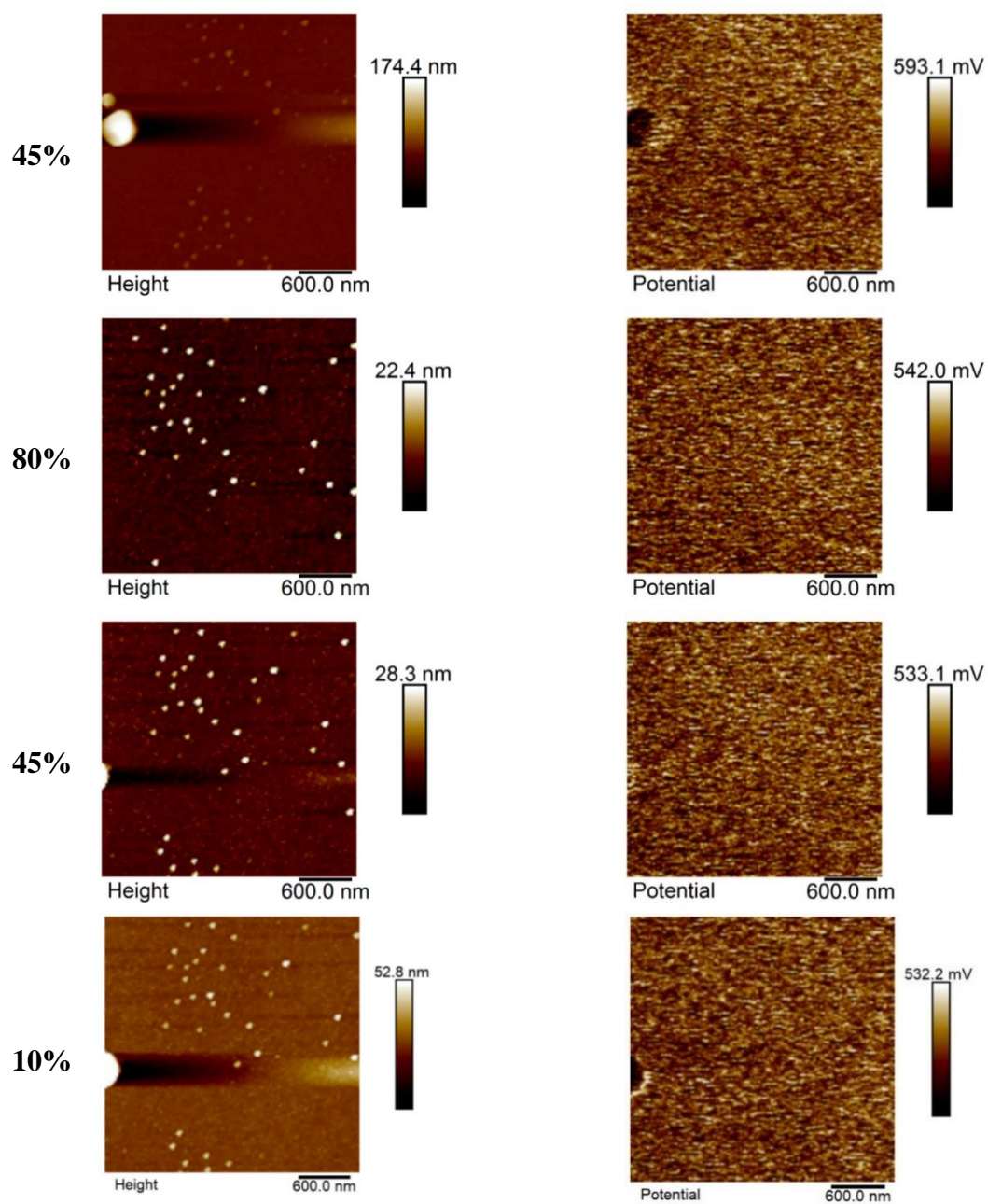


Figure 54. AFM images of topography (left) and potential map (right) of the sample #3 during the third measurement cycle 45%-80%-45%-10%.

The sample surface for 10% RH and 80% RH obtaining using an OM is shown in Figure 55. There is no difference between them, as it was for previous sample #2. It means that also this sample does not expand with moisture.

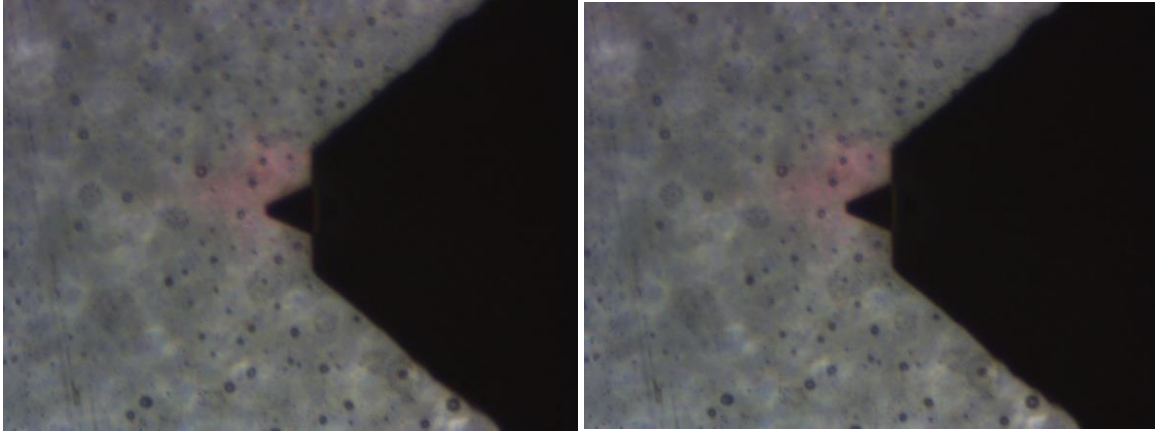


Figure 55. Photographs of the sample #3 surface for 10% RH (left) and 80% RH (right) using an OM. Optical resolution is 500x375  $\mu\text{m}$ .

Gaussian peak functions of potential for three cycles are presented in Figure 56. On the first cycle (Figure 56 (a)) the central potential value is increasing with 13% - 45% RH change and after decreasing during any RH changes. Peaks have the largest amplitude at 13% and 10% RH. The central potential value is increasing during the second cycle (Figure 56 (b)) except the 45% - 80% RH change. However, the third cycle (Figure 56 (c)) has an opposite correlation. The central potential value is decreasing except the 45% - 80% change, where it goes up.

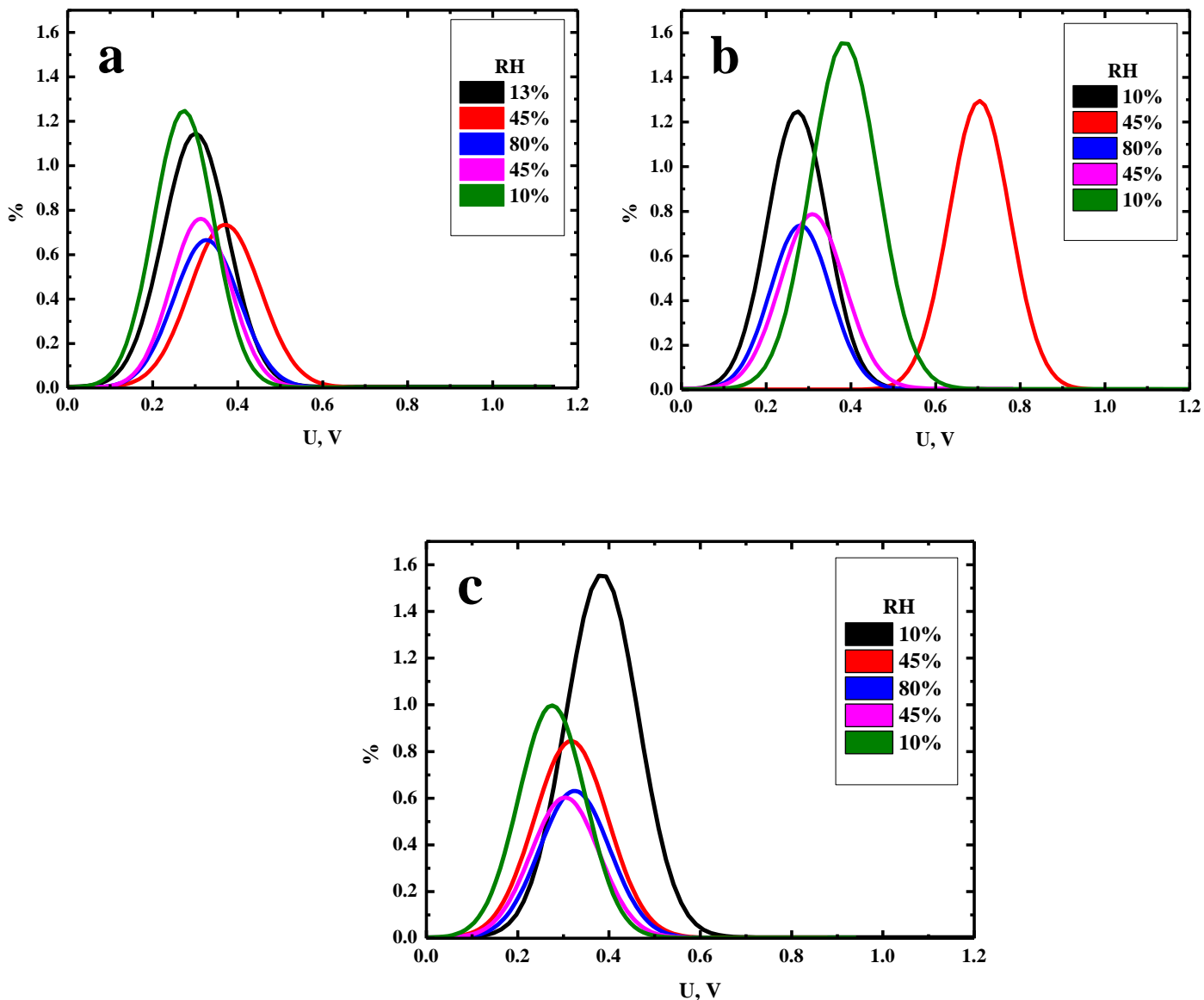


Figure 56. Gaussian peak functions of electric potential during the RH changing of the sample #3. (a) the first cycle; (b) the second cycle; (c) the third cycle.

Table 5 shows the main parameters of the Gaussian peaks for all measurements for sample #3. This allows the analysis of the potential distribution.

Table 6 shows the change in electric potential during measurements. It represents the differences in the parameters' values between the previous measurement and the next one, i.e.  $A=A_i - A_{i+1}$ , where  $i$  is the serial number of measurement. Thus, the negative value in the table means that the parameter value has increased.

Table 5. The main parameters of the Gaussian peaks for all measurements of the sample #3.

RH	Parameters	1 cycle	2 cycle	3 cycle
10%	$x_c$	0.301	0.273	0.385
	$A$	1.141	1.245	1.556
	$FWHM$	0.180	0.166	0.188
45%	$x_c$	0.371	0.704	0.317
	$A$	0.732	1.293	0.844
	$FWHM$	0.196	0.170	0.190
80%	$x_c$	0.327	0.281	0.325
	$A$	0.665	0.735	0.631
	$FWHM$	0.181	0.167	0.181
45%	$x_c$	0.313	0.309	0.304
	$A$	0.760	0.782	0.601
	$FWHM$	0.166	0.179	0.176
10%	$x_c$	0.273	0.385	0.275
	$A$	1.245	1.556	0.996
	$FWHM$	0.166	0.188	0.172

Table 6. The differences in the parameters' values between the previous measurement and the next one for the sample #3.

Parameters	RH	1 cycle	2 cycle	3 cycle
$x_c$	10% - 45%	-0.070	-0.430	0.068
	45% - 80%	0.044	0.423	-0.008
	80% - 45%	0.014	-0.028	0.021
	45% - 10%	0.039	-0.076	0.029
$A$	10% - 45%	0.409	-0.049	0.712
	45% - 80%	0.067	0.559	0.213
	80% - 45%	-0.096	-0.047	0.030
	45% - 10%	-0.485	-0.774	-0.396
$FWHM$	10% - 45%	-0.016	-0.004	-0.002
	45% - 80%	0.015	0.002	0.009
	80% - 45%	0.015	-0.012	0.005
	45% - 10%	-7E-05	-0.009	0.004

Figure 57 shows change in the position of the maximum of the Gaussian curve during the change in RH for three measurement cycles. The presented graphs take into account the influence of the probe on the potential change. It was done by subtracting the average value

of copper and aluminum foils potential from the obtained values. The curve behavior of the 1<sup>st</sup> and the 3<sup>rd</sup> cycles are similar, but changes are small. However, the amplitude of changes of the central value is high during the 2<sup>nd</sup> cycle, and its behavior is comparable with the 1<sup>st</sup> cycle of measurement of the 2<sup>nd</sup> sample.

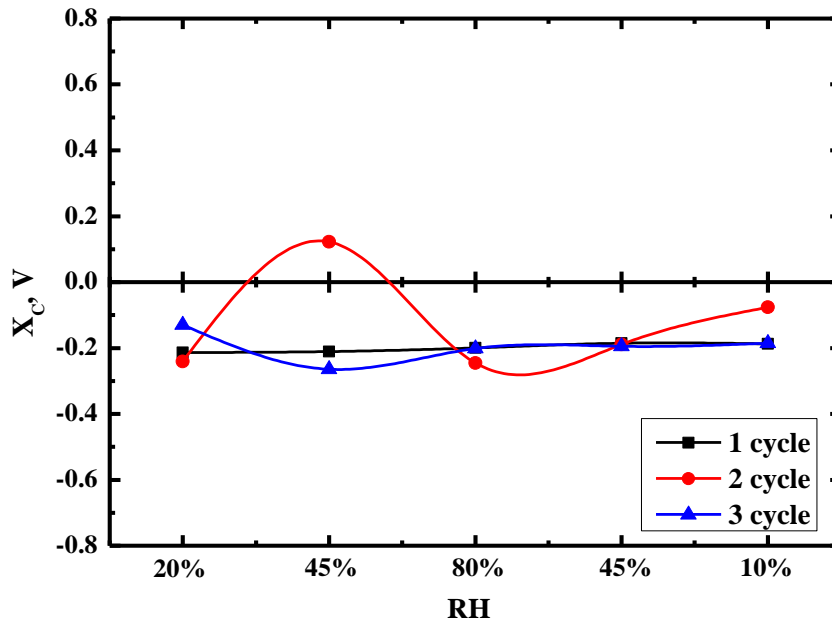


Figure 57. Change in the position of the maximum of the Gaussian curve during the change in RH for three measurement cycles of the sample #3.

In the course of the obtained results, no strict correlation was found between the potential and the RH change. However, the work of Adamchuck *et al.*, 2020, showed that the most conductive sample reacts more strongly to changes in air humidity. In our case, sample #1 was the most conductive and the measurement results of this sample were close to the results obtained in the work of Adamchuck *et al.*, 2020. Resistivity (in our case, potential) fell down (Figure 21 and Figure 45) during the RH changing from 0% to 30% (in our case, from 10% RH to 45% RH). After this the resistivity is increasing till 100% RH (80% for sample #1), and again decreasing with humidity reduction.

## 5. Conclusion

In the course of work on the master's thesis, literature in a related field of research was studied. The basic principles of AFM operation were learnt and practical skills of working with it were obtained. The samples were prepared for measurements and the experiments were carried out. It was required to get acquainted with the software (The NanoScope software, Bruker) that is used on Multimode 8 (Bruker) microscope during the measurements and post-processing. The processing of the results included the basic principles of small-order data filtering and editing the obtained images.

Within the framework of this thesis, three samples based on tin dioxide were investigated. Each sample measurement consists of 3 cycles of changing RH. During each cycle RH was changed from 10% to 80% and then back to 10%, so one cycle is 10% - 40% - 80% - 40% - 10% RH. Three cycles were done for checking the repeatability of the results. The measurement cycles showed different results, which indicates poor reproducibility of the experiment.

All three samples were made from tin dioxide film with different concentration of oxygen in argon-oxygen plasma during reactive magnetron sputtering. One and two nickel strips were used during the sputtering as ferromagnetic inserts to the target. Additionally, samples have different resistivity. Sample #1 has the smallest resistance and sample #2 has the highest resistance.

PeakForce KPFM mode was used for potential measurement. This work presents the topography and the electric potential map of the three samples under study. The depth histogram of the electric potential and its amplitude version of the Gaussian peak function were built in order to better understand the dependence of the electric potential value changes to RH changing. It should be noted that the influence of the probe on the measurements was also considered, which develops the previous research findings on that subject by our group. For this purpose, similar measurements were carried out on aluminum and copper foils. The obtained data was used to plot the changes in the position of the maximum of the Gaussian curve.

In the course of the obtained results, no strict correlation was found between the electric potential and the RH change. However, the potential value still changes with different RH values. The hypothesis put forward was confirmed: the potential value shifts with changes

in humidity. The AFM was used to measure the potential on the sample surface. Particle analysis showed a relative displacement of the potential with changes in RH. The central value of the Gaussian curves varied in the range of 0.005-0.76 V relative to the earlier value. The largest shift of the center value during the measurement of one sample was 0.97 V for sample #2.

This research should be continued because there are more unstudied materials and more methods that can be applied to investigate the phenomenon. Also, there are still some improvements that can be made during the experiment to obtain better results.

The films studied in the framework of this master's thesis were deposited on a glass substrate, which is non-conductive. In this regard, the sample was fixed on a metal substrate using a conductive paste, and a contact track was also made, connecting this substrate to the film. However, there may still be air gaps between the layers, which would affect the measurement results. To prevent this effect and to increase conductivity, samples should be made thinner, or some composites should be added, e.g., carbon nanotubes. Additional compositional studies using X-ray diffraction, magnetic properties using magnetic force microscopy and SQUID would help to study materials in more detail and evaluate what may affect the change in potential.

One of the difficulties in the course of measurements was the setting of RH, since the humidity control setup takes a long time to set the required level. Also, humidity value slightly changes during the air surge in the chamber, which may be associated with fluctuations in the dry air flow supplied from the central system of the university. For future experiments, it is recommended to modify the installation to more accurately change the humidity level. During scanning, the RH in the gas cell drops due to the fact that at this time no air is supplied to the cell. A sealed cell or a sealed chamber around the setup would be required to prevent unwanted humidity fluctuations. Changing scan settings also can lead to better results and lower noise in the final images.

## References

- Adamchuck, D. V. *et al.* (2020) 'Features of water vapor adsorption and desorption on the surface of non-stoichiometric tin dioxide films', *Proceedings of the National Academy of Sciences of Belarus. Physics and Mathematics Series*, 56(1), pp. 102 – 113. doi: 10.29235/1561-2430-2020-56-1-102-113.
- Cardellach i Redon, M. (2013) *Study of interfacial water at the nanoscale at ambient conditions with SPM*. Universitat Autònoma de Barcelona. Available at: <https://ddd.uab.cat/record/114025> (Accessed: 10 March 2021).
- Davydov, S. Yu., Moshnikov, V. A. and Fedotov, A. A. (2006) 'Adsorption of oxygen molecules and carbon monoxide molecules on tin dioxide', *Technical Physics*, 51(1), pp. 139 – 141. doi: 10.1134/S1063784206010221.
- Doroshkevich, A. S. *et al.* (2017) 'Nonequilibrium chemo-electronic conversion of water on the nanosized YSZ: experiment and Molecular Dynamics modelling problem formulation', *Journal of Physics: Conference Series*, 848, p. 012021. doi: 10.1088/1742-6596/848/1/012021.
- Doroshkevich, A. S. *et al.* (2019) 'Direct conversion of the water adsorption energy to electricity on the surface of zirconia nanoparticles', *Applied Nanoscience*, 9(8), pp. 1603 – 1609. doi: 10.1007/s13204-019-00979-6.
- Ducati, T. R. D., Simões, L. H. and Galembeck, F. (2010a) 'Charge Partitioning at Gas–Solid Interfaces: Humidity Causes Electricity Buildup on Metals', *Langmuir*, 26(17), pp. 13763 – 13766. doi: 10.1021/la102494k.
- Ducati, T. R. D., Simões, L. H. and Galembeck, F. (2010b) 'Charge Partitioning at Gas–Solid Interfaces: Humidity Causes Electricity Buildup on Metals', *Langmuir*, 26(17), pp. 13763–13766. doi: 10.1021/la102494k.
- Etzler, F. M. and Drelich, J. (2012) 'Atomic Force Microscopy for Characterization of Surfaces, Particles, and Their Interactions', *Developments in Surface Contamination and Cleaning: Detection, Characterization, and Analysis of Contaminants*, pp. 307 – 331. doi: 10.1016/B978-1-4377-7883-0.00006-7.
- Giessibl, F. J. (2003) 'Advances in atomic force microscopy', *Rev. Mod. Phys.*, 75(3), p. 35.
- Gouveia, R. F. and Galembeck, F. (2009) 'Electrostatic charging of hydrophilic particles due to water adsorption', *Journal of the American Chemical Society*, 131(32), pp. 11381 – 11386. doi: 10.1021/ja900704f.
- Help Online - Origin Help - GaussAmp* (no date). Available at: <https://www.originlab.com/doc/Origin-Help/GaussAmp-FitFunc> (Accessed: 2 April 2021).
- Jalili, N. and Laxminarayana, K. (2004) 'A review of atomic force microscopy imaging systems: application to molecular metrology and biological sciences', *Mechatronics*, 14(8), pp. 907 – 945. doi: 10.1016/j.mechatronics.2004.04.005.

Kaemmer, S. B. (2011) ‘Application note #133. Introduction to Bruker’s ScanAsyst and PeakForce Tapping AFM Technology’. Bruker, USA.

*Kelvin Probe Force Microscopy (KPFM)* (no date). Available at: <https://www.parksystems.com/park-spm-modes/93-dielectric-piezoelectric/232-kelvin-probe-force-microscopy-kpfm> (Accessed: 10 March 2021).

Liu, Xiaomeng *et al.* (2020) ‘Power generation from ambient humidity using protein nanowires’, *Nature*, 578(7796), pp. 550 – 554. doi: 10.1038/s41586-020-2010-9.

Lovley, D. R. *et al.* (2011) ‘Geobacter: The Microbe Electric’s Physiology, Ecology, and Practical Applications’, in Poole, R. K. (ed.) *Advances in Microbial Physiology*. Academic Press (Advances in Microbial Physiology), pp. 1 – 100. doi: 10.1016/B978-0-12-387661-4.00004-5.

Marrese, M., Guarino, V. and Ambrosio, L. (2017) ‘Atomic Force Microscopy: A Powerful Tool to Address Scaffold Design in Tissue Engineering’, *Journal of Functional Biomaterials*, 8(1). doi: 10.3390/jfb8010007.

Martin, Y., Williams, C. C. and Wickramasinghe, H. K. (1987) ‘Atomic force microscope–force mapping and profiling on a sub 100-Å scale’, *Journal of Applied Physics*, 61(10), pp. 4723 – 4729. doi: 10.1063/1.338807.

Melitz, W. *et al.* (2011) ‘Kelvin probe force microscopy and its application’, *Surface Science Reports*, 66(1), pp. 1 – 27. doi: 10.1016/j.surfrep.2010.10.001.

*Metals and Alloys - Melting Temperatures* (no date). Available at: [https://www.engineeringtoolbox.com/melting-temperature-metals-d\\_860.html](https://www.engineeringtoolbox.com/melting-temperature-metals-d_860.html) (Accessed: 1 May 2021).

Mironov, V. (2004) *Fundamentals of Scanning Probe Microscopy*. Nizhniy Novgorod: NT-MDT.

Mohammadi, N. (2017) *Humidity to electricity converter based on zirconia nano-particles*. Master’s thesis. Lappeenranta University of Technology.

Nonnenmacher, M., O’Boyle, M. P. and Wickramasinghe, H. K. (1991) ‘Kelvin probe force microscopy’, *Applied Physics Letters*, 58(25), pp. 2921 – 2923. doi: 10.1063/1.105227.

*PeakForce QNM* (no date). Available at: <https://www.bruker.com/en/products-and-solutions/microscopes/materials-afm/afm-modes/peakforce-qnm.html> (Accessed: 1 May 2021).

*Piezoelectric Scanners* (no date). Available at: <http://nanophys.kth.se/nanophys/facilities/nfl/afm/icon/bruker-help/Content/SPM%20Training%20Guide/Piezoelectric%20Scanners/Piezoelectric%20Scanners.htm> (Accessed: 10 March 2021).

*Probes - Bruker AFM Probes* (no date). Available at: <https://www.brukerafmprobes.com/c-15-probes.aspx> (Accessed: 2 May 2021).

Rasheed, A. (2017) *Effect of humidity on electric potential of ZrO<sub>2</sub> nanocomposite investigated by AFM / KPFM*. Master's thesis. Lappeenranta University of Technology.

Rugar, D. and Hansma, P. (1990) 'Atomic Force Microscopy', *Physics Today*, 43(10), pp. 23 – 30. doi: 10.1063/1.881238.

Seo, Y. and Jhe, W. (2008) 'Atomic force microscopy and spectroscopy', *Reports on Progress in Physics*, 71(1), p. 016101. doi: 10.1088/0034-4885/71/1/016101.

Verma, A. S. and Singh, A. (2020) *Animal Biotechnology: Models in Discovery and Translation*. Elsevier.

Young, T. J. *et al.* (2011) 'The use of the PeakForce™ quantitative nanomechanical mapping AFM-based method for high-resolution Young's modulus measurement of polymers', *Measurement Science and Technology*, 22(12), p. 125703. doi: 10.1088/0957-0233/22/12/125703.

Yulianto, B., Gumilar, G. and Septiani, N. L. W. (2015) 'SnO<sub>2</sub> Nanostructure as Pollutant Gas Sensors: Synthesis, Sensing Performances, and Mechanism', *Advances in Materials Science and Engineering*, 2015, pp. 1 – 14. doi: 10.1155/2015/694823.

Yurakov, Yu. A. *et al.* (2007) 'Образование Окислов В Нанослоях Олова', *Конденсированные Среды И Межфазные Границы*, 9(4). Available at: <https://www.elibrary.ru/item.asp?id=11902617> (Accessed: 1 May 2021).

*Z Feedback Loop* (no date). Available at: <http://nanophys.kth.se/nanophys/facilities/nfl/afm/icon/bruker-help/Content/SPM%20Training%20Guide/Z%20Feedback%20Loop.htm> (Accessed: 10 March 2021).